FRONTIERS OF PHYSICS

RESEARCH ARTICLE
Volume 21 / Issue 11 / 115201 / 2026

Parity detection based on non-Hermitian spectral phase transition

Yang Xiao[1], Hao-Long Zhang[1], Ri-Hua Zheng[1], Jie Song[3], Ye-Hong Chen[1,4,†], Yi-Hao Kang[2,‡], Yan Xia[1,§]

1 Fujian Key Laboratory of Quantum Information and Quantum Optics, College of Physics and Information Engineering, Fuzhou University, Fuzhou 350108, China
2 School of Physics, Hangzhou Normal University, Hangzhou 311121, China
3 Department of Physics, Harbin Institute of Technology, Harbin 150001, China
4 Quantum Information Physics Theory Research Team, Center for Quantum Computing, RIKEN, Wako-shi, Saitama 351-0198, Japan
Corresponding authors. E-mail: †yehong.chen@fzu.edu.cn, ‡yihaokang@hznu.edu.cn, §xia-208@163.com
Received November 15, 2025; accepted February 6, 2026

ABSTRACT

We present a protocol for realizing parity detection of a bipartite system based on non-Hermitian spectral phase transition. The system comprises two superconducting qubits as information carriers and an auxiliary superconducting resonator. We derive a parity-dependent effective Hamiltonian, where the frequency of the resonator is shifted when the qubits are in even-parity states. The frequency shift results in a spectral phase transition in the non-Hermitian dynamical matrix in the Heisenberg picture, where the spectrum turns from purely imaginary to purely real. With a proper frequency shift, the spectral distinction between the even- and odd-parity cases leads to markedly different photon number dynamics, i.e., exponential growth for the odd-parity case, and bounded oscillations for the even-parity case. By measuring the photon number in the resonator after a fixed evolution time, the parity of the qubits can be reliably discriminated. Numerical simulations further demonstrate that the protocol is robust against systematic imperfections and decoherence, including the spontaneous emission and dephasing of the qubits, as well as cavity decay. These results establish a practical route to parity detection via non-Hermitian dynamics. This approach provides a scalable building block for superconducting-circuit quantum information processing.

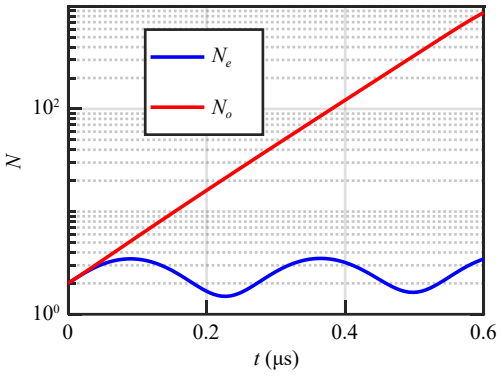

Keywords non-Hermitian systems, superconducting devices, quantum information processing

1 Introduction

In recent years, non-Hermitian dynamics has attracted increasing attention in various physical systems [1–25], particularly in superconducting systems [13–15, 26], photonic systems [16–18, 24], and magnetic systems [19–22], where the rich and unconventional physical phenomena of the non-Hermitian dynamics have been revealed gradually. In contrast to Hermitian dynamics, within the realm of non-Hermitian dynamics, the system

*Special Topic: Non-Hermitian Physics (Eds.: Peng Xue, Lan Yang & Wu-Ming Liu).

Higher Education Press

https://doi.org/10.15302/frontphys.2026.115201

can possess complex energy spectra, enabling phenomena such as spectral phase transitions, exceptional points, and chiral dynamics [27–30]. These features offer new opportunities for exploring quantum behaviors beyond equilibrium [7–9], and exhibit novel applications in quantum information tasks like quantum state manipulation [31–33], signal detection, quantum precision measurements [34–36], chiral mode switching [28–30, 37–43], and nonreciprocal transport [44–48]. Recent studies [14, 31, 32, 34, 35] have further shown that quantum information schemes based on non-Hermitian dynamics offer many potential advantages over their counterparts within the realm of Hermitian dynamics.

To realize non-Hermitian dynamics, a common approach suggests to design a non-Hermitian effective Hamiltonian by coupling a quantum system to a thermal reservoir with gain or loss [27, 49–53]. However, this approach poses several challenges. For instance, the reservoir-induced decoherence can obscure non-Hermitian signatures, making it difficult to stably observe coherent non-Hermitian effects [32, 49, 54]. Moreover, interactions between the system and reservoir may trigger quantum jumps, driving the system evolution away from the ideal trajectory governed by the non-Hermitian Hamiltonian [55, 56]. As a result, post-selection is necessary to exclude the occurrence of quantum jumps, leading to probabilistic implementations of non-Hermitian dynamics.

To overcome these challenges, alternative approaches that do not rely on post-selection have been proposed [55, 57–65], such as the approaches make use of non-Hermitian dynamical matrices in the Heisenberg picture [57, 58] and Liouvillian superoperator formalism [55, 59–65]. In particular, the Heisenberg-picture-based approach provides a way to realize non-Hermitian dynamics without invoking any explicit dissipation. In such schemes [57, 58], the non-Hermitian nature is embedded in the dynamical matrices of operators, and spectral phase transitions can emerge by tuning system parameters. The resultant spectral phase transitions delineate dynamical regimes characterized by distinct symmetries. This inherent connection facilitates direct symmetry probing through dynamical observables, such as parity detection via photon number monitoring, without the need for engineered dissipation or post-selection. In contrast to conventional methods that infer symmetry from fragile indicators like state populations, the non-Hermitian framework significantly improves the robustness of the measurement against errors and decoherence [66, 67].

Parity detection is a widely used primitive in quantum information processing [68]. It serves as a key ingredient in tasks such as Bell-state analysis and entanglement generation in quantum communication, and it also underlies stabilizer-based protocols where parity outcomes provide syndrome information for error detection and correction [69, 70]. Motivated by these applications, we explore parity detection from a non-Hermitian dynamical perspective in this work.

In this paper, we propose a protocol for parity detection of a bipartite system based on non-Hermitian spectral phase transition. The physical model consists of two superconducting qubits and a superconducting resonator. The qubits serve as the information carriers, while the resonator acts as an auxiliary element in the parity detection. The resonator is simultaneously coupled to both qubits and is driven by a two-photon drive. Based on this physical model, we derive a parity-dependent effective Hamiltonian of the system, where the resonator's frequency shifts when the qubits are in even-parity states.

Under the derived effective Hamiltonian, we analyze the evolution of the resonator's creation and annihilation operators in the Heisenberg picture using the Heisenberg equation of motion. When the qubits are in odd-parity states, the non-Hermitian dynamical matrix, which characterizes the evolution of the creation and annihilation operators, exhibits a purely imaginary spectrum. However, the frequency shift of the resonator induced by the qubits in even-parity states introduces an additional diagonal term in the non-Hermitian dynamical matrix. By tuning the absolute value of this frequency shift from zero to values greater than the strength of the two-photon drive, we observe that the spectrum of the dynamical matrix turns from purely imaginary to purely real. This marks a spectral phase transition of the non-Hermitian dynamical matrix.

We further demonstrate that this spectral phase transition can be utilized to achieve effective parity detection for the two qubits. More specifically, by selecting appropriate control parameters of the system, we introduce a frequency shift in the resonator for the even-parity case, ensuring that the non-Hermitian dynamical matrix exhibits a purely real spectrum. In contrast, for the odd-parity case, the absence of a frequency shift causes the dynamical matrix to retain a purely imaginary spectrum. The disparity between these dynamical matrices leads to distinct variations in photon number. In the even-parity case, the purely real spectrum ensures that the average photon number in the resonator oscillates with a finite upper bound. Conversely, in the odd-parity case, the purely imaginary spectrum results in an exponential increase in the photon number within the resonator over time. After a specific evolution period, the photon number of the resonator can serve as a criterion for extracting the parity information of the qubits. By measuring the photon number, one can differentiate between the even- and odd-parity states of the qubits.

To investigate the performance of the protocol in the presence of potential experimental imperfections, we conduct numerical simulations using available parameters. The results show that the parity detection based on

non-Hermitian spectral phase transition is robust against systematic errors and decoherence, including spontaneous emission and dephasing of the qubits, as well as cavity decay. The protocol may provide an alternative method to achieve high-precision parity detection using currently feasible technology.

It is instructive to compare our parity detection protocol with alternative parity readout approaches in superconducting platforms. Conventional dispersive schemes typically map parity onto a probe field (or an ancilla) through dispersive coupling and then infer parity via homodyne/ancilla readout [68], while gate-based parity checks extract the parity syndrome onto an ancilla using multi-qubit gate sequences (as commonly used in error-correction settings) [69, 70]. Interferometric strategies encode parity in interference contrast but may require additional hardware resources. In contrast, our approach exploits a parity-dependent spectral phase transition of a non-Hermitian dynamical matrix in the Heisenberg picture, which maps parity directly onto two sharply different photon-number dynamics (bounded versus amplifying), enabling a simple threshold decision. This dynamical mapping does not require post-selection and remains robust against typical systematic imperfections and decoherence channels analyzed in Section 5.

This article is organized as follows. In Section 2, we introduce the physical model and calculate the effective Hamiltonian. Theoretical analysis for the energy spectra of non-Hermitian dynamic matrices is given in Section 3. In Section 4, we provide the details of the parity detection based on non-Hermitian spectral phase transition. In Section 5, we investigate the influence of the disturbing factors, including systematic errors and decoherence, on the protocol. Finally, the conclusions are given in Section 6.

2 Physical model

Let us now introduce the physical model to implement the parity detection based on non-Hermitian spectral phase transition. We consider a physical model composed of two superconducting qubits q_n $(n=1,2)$ [71–76] and a superconducting resonator C [77–79], as shown in Fig. 1. The lowest two levels of the qubit q_n are labeled as $|g\rangle_n$ and $|e\rangle_n$. The frequency of the transition $|g\rangle_n \leftrightarrow |e\rangle_n$ and the resonator C are denoted as ω_n and ω_c, respectively. The transition $|g\rangle_n \leftrightarrow |e\rangle_n$ is coupled with the mode in the resonator C with the coupling strength λ_n and the blue detuning $\Delta_n = \omega_c - \omega_n$. In addition, the resonator is subjected to a two-photon driving field with amplitude ξ. The Hamiltonian of the system under the rotating-wave approximation is

$$H = \mathrm{i}\xi(a^{\dagger 2} - a^2) + \sum_{n=1}^{2} (\lambda_n \mathrm{e}^{\mathrm{i}\Delta_n t} a^\dagger |g\rangle_n\langle e| + \mathrm{H.c.}), \quad (1)$$

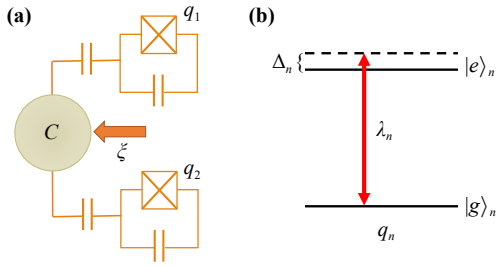

Fig. 1 **(a)** Physical model for the implementation of the parity detection consisting of two qubits and a superconducting resonator. **(b)** Level configuration of the qubit q_n $(n=1,2)$.

where a $(a^\dagger)$ is the annihilation (creation) operator of the mode in the resonator C. We note that the term $\mathrm{i}\xi(a^{\dagger 2} - a^2)$ corresponds to a particular choice of the pump phase of the two-photon drive; the parity dependent spectral phase transition discussed in this work is independent of this phase, and the real-coefficient form $\xi(a^{\dagger 2} + a^2)$ is discussed in Appendix B.

For clarity, we separate Eq. (1) as $H(t) = H_d + V(t)$, where the two-photon drive $H_d = \mathrm{i}\xi(a^{\dagger 2} - a^2)$ is time independent and acts only on the resonator, while the time-dependent qubit–resonator coupling $V(t)$ is treated perturbatively. Considering the second-order perturbation theory [80] in the dispersive regime $\Delta_n \gg \{\lambda_n, \xi\}$, the effective Hamiltonian can be calculated as

$$H_e = \mathrm{i}\xi(a^{\dagger 2} - a^2) + \sum_{n=1}^{2} \frac{\lambda_n^2}{\Delta_n} (a^\dagger a |g\rangle_n\langle g| - a^\dagger a |e\rangle_n\langle e| - |e\rangle_n\langle e|). \quad (2)$$

The detailed derivation of Eq. (2) is given in Appendix A. Defining $\delta_n = \lambda_n^2/\Delta_n$ and choosing $\delta_1 = \delta_2 \equiv \delta$, Eq. (2) can be simplified as

$$\begin{aligned} H_{\mathrm{eff}} &= H_d + H_q, \\ H_d &= \mathrm{i}\xi(a^{\dagger 2} - a^2) + 2\delta(|g,g\rangle_{1,2}\langle g,g| - |e,e\rangle_{1,2}\langle e,e|)a^\dagger a, \\ H_q &= -\delta(|e,g\rangle_{1,2}\langle e,g| + |g,e\rangle_{1,2}\langle g,e| + 2|e,e\rangle_{1,2}\langle e,e|). \end{aligned} \quad (3)$$

Here $|g,g\rangle_{1,2} \equiv |g\rangle_1 \otimes |g\rangle_2$, $|e,g\rangle_{1,2} \equiv |e\rangle_1 \otimes |g\rangle_2$, $|g,e\rangle_{1,2} \equiv |g\rangle_1 \otimes |e\rangle_2$, and $|e,e\rangle_{1,2} \equiv |e\rangle_1 \otimes |e\rangle_2$. Because $[H_q, H_d] = 0$ and H_q is independent of the resonator mode, H_q does not affect the dynamical evolution of the resonator operators and can be omitted when focusing on the resonator dynamics. Physically, Eq. (2) shows that each qubit induces an AC-Stark (dispersive) shift of the resonator frequency of magnitude $\delta_n = \lambda_n^2/\Delta_n$, with opposite signs for $|g\rangle_n$ and $|e\rangle_n$. As a result, the total shift adds constructively in the even-parity subspaces (yielding $\bar{\delta} = \pm\delta$), while it cancels in the odd-parity subspace when $\delta_1 = \delta_2$ (yielding $\bar{\delta} = 0$).

3 Dynamical matrices and their spectra

3.1 Theoretical analysis

In order to investigate the dynamical evolution of the resonator mode, we focus on a reduced effective Hamiltonian of the resonator in form of

$$\bar{H} = \mathrm{i}\xi(a^{\dagger 2} - a^2) + 2\bar{\delta}a^\dagger a. \tag{4}$$

We define the subspaces for the two-qubit states as

$$\begin{aligned} &\mathcal{S}_+ = \mathrm{span}\{|g,g\rangle_{1,2}\},\ \mathcal{S}_- = \mathrm{span}\{|e,e\rangle_{1,2}\},\\ &\mathcal{S}_0 = \mathrm{span}\{|e,g\rangle_{1,2}, |g,e\rangle_{1,2}\}. \end{aligned} \tag{5}$$

When the state of the qubits are initial in subspace $\mathcal{S}_\pm$ ($\mathcal{S}_0$), the effective Hamiltonian in Eq. (3) reduces to $\bar{H}$ with $\bar{\delta} = \pm\delta$ ($\bar{\delta} = 0$). Therefore, the Hamiltonian $\bar{H}$ can represent the evolution of the resonator mode for the qubits prepared in the subspace $\mathcal{S}_0$ and $\mathcal{S}_\pm$, by substituting different values into the parameter $\bar{\delta}$.

Based on the reduced effective Hamiltonian $\bar{H}$ in Eq. (4), we move into the Heisenberg picture, where the evolution of the annihilation and creation operators of the resonator are given by the Heisenberg equation of motion as

$$\begin{aligned} &\mathrm{i}\dot{a} = 2\bar{\delta}a + 2\mathrm{i}\xi a^\dagger,\\ &\mathrm{i}\dot{a}^\dagger = 2\mathrm{i}\xi a - 2\bar{\delta}a^\dagger. \end{aligned} \tag{6}$$

Additionally, we define the vector $\boldsymbol{v}(t)$ as $[a(t), a^\dagger(t)]^{\mathrm{T}}$, where the superscript T represents the matrix transpose. Thus, one can obtain a Schrödinger-like equation

$$\mathrm{i}\frac{\mathrm{d}}{\mathrm{d}t}\boldsymbol{v}(t) = \mathcal{H}\boldsymbol{v}(t), \tag{7}$$

with the dynamical matrix given by

$$\mathcal{H} = \begin{pmatrix} 2\bar{\delta} & 2\mathrm{i}\xi \\ 2\mathrm{i}\xi & -2\bar{\delta} \end{pmatrix}. \tag{8}$$

Eq. (8) indicates that the dynamical matrix $\mathcal{H}$ is non-Hermitian. We emphasize that the non-Hermiticity discussed in this work does not originate from a change of picture, nor does it imply that the Hamiltonian governing the system is non-Hermitian. Throughout this work, the system is described by a Hermitian Hamiltonian in the Schrödinger picture and thus exhibits unitary time evolution in the absence of dissipation. The non-Hermitian structure instead arises from the form of the Heisenberg equations of motion. For quadratic, number-nonconserving Hamiltonians, the Heisenberg equations for the bosonic operators can be written as a closed set of linear differential equations, which can be expressed compactly in a matrix form. The matrix $\mathcal{H}$ appearing in Eq. (8) is therefore a dynamical matrix governing the linear operator evolution, rather than a Schrödinger-picture Hamiltonian. As a consequence, this dynamical matrix is not required to be Hermitian, even though the underlying quantum dynamics remains fully unitary. The non-Hermitian spectral properties of $\mathcal{H}$ thus reflect the structure of the operator equations of motion, rather than indicating any non-unitary physical evolution of the closed system. Similar non-Hermitian dynamical matrices in nondissipative bosonic systems have been discussed previously, see, e.g., Ref. [57].

To further analyze the symmetry of the dynamical matrix $\mathcal{H}$, we rewrite it as

$$\mathcal{H} = 2\mathrm{i}\xi\sigma_x + 2\bar{\delta}\sigma_z, \tag{9}$$

by employing the Pauli matrices

$$\sigma_x = \begin{pmatrix} 0 & 1 \\ 1 & 0 \end{pmatrix},\ \sigma_y = \begin{pmatrix} 0 & -\mathrm{i} \\ \mathrm{i} & 0 \end{pmatrix},\ \sigma_z = \begin{pmatrix} 1 & 0 \\ 0 & -1 \end{pmatrix}. \tag{10}$$

For the dynamical matrix $\mathcal{H}$, the parity operator is defined as $\mathcal{P} = \sigma_z$, while the time-reversal operator is given by $\mathcal{T} = *$, representing complex conjugation operator [81–87]. Here $\mathcal{T} = *$ denotes the conventional time-reversal operation for spinless (bosonic) systems, which is appropriate for the dynamical matrix formulated in the $[a, a^\dagger]^{\mathrm{T}}$ operator basis. For an arbitrary matrix Q and an arbitrary vector $\boldsymbol{v}(t)$, the time-reversal operator produces the results $\mathcal{T}Q\mathcal{T} = Q^*$ and $\mathcal{T}\boldsymbol{v}(t) = \boldsymbol{v}^*(t)$. The operators $\mathcal{P}$ and $\mathcal{T}$ satisfy the commutation relation $[\mathcal{P}, \mathcal{T}] = 0$. The dynamical matrix $\mathcal{H}$ exhibits $\mathcal{PT}$ symmetry, as it satisfies the commutation relation $[\mathcal{PT}, \mathcal{H}] = 0$.

The spectrum of the dynamical matrix $\mathcal{H}$ directly governs the time dependence of the operator vector $\boldsymbol{v}(t)$ via $\boldsymbol{v}(t) = \mathrm{e}^{-\mathrm{i}\mathcal{H}t}\boldsymbol{v}(0)$. Consequently, when the eigenvalues are real, the evolution is oscillatory and the resonator photon number remains bounded, whereas imaginary eigenvalues produce exponential amplification/attenuation and lead to an exponentially growing (or decaying) photon number. Therefore, a spectral phase transition of $\mathcal{H}$ implies a qualitative change in the physical photon-number dynamics. Introducing the parameter $d = \xi/\bar{\delta}$, we summarize the relationship between the energy spectrum of the dynamical matrix $\mathcal{H}$ and the parameter d as follows:

(i) For $|d| < 1$, the eigenvectors of the Hamiltonian $\mathcal{H}$ are given by

$$|\phi_\pm\rangle = \frac{1}{\sqrt{\mathcal{N}_\pm}} \begin{pmatrix} 1 \pm \sqrt{1-d^2} \\ \mathrm{i}d \end{pmatrix}, \tag{11}$$

where the normalization coefficients are $\mathcal{N}_\pm = 2(1 \pm \sqrt{1-d^2})$, and the corresponding eigenvalues are $E_\pm = \pm 2\bar{\delta}\sqrt{1-d^2}$. Since the eigenvectors satisfy $\mathcal{PT}|\phi_\pm\rangle = \pm|\phi_\pm\rangle$, the eigenvectors $|\phi_\pm\rangle$ of $\mathcal{H}$ is also the eigenvectors of the $\mathcal{PT}$ operator. This indicates that $\mathcal{PT}$-

symmetry remains unbroken, and the eigenvalues $E_\pm$ are purely real.

(ii) For $|d|>1$, the eigenvectors of the Hamiltonian $\mathcal{H}$ take the form

$$|\phi_\pm\rangle = \frac{1}{\sqrt{2}d}\begin{pmatrix} 1 \pm \mathrm{i}\sqrt{d^2-1} \\ \mathrm{i}d \end{pmatrix}, \tag{12}$$

with purely imaginary eigenvalues $E_\pm = \pm 2\mathrm{i}\bar{\delta}\sqrt{d^2-1}$. Furthermore, the eigenvectors do not satisfy $\mathcal{PT}|\phi_\pm\rangle = \pm|\phi_\pm\rangle$, which implies that the eigenvectors of $\mathcal{H}$ are no longer the eigenvectors of the $\mathcal{PT}$ operator. Consequently, the $\mathcal{PT}$-symmetry is broken in this case.

(iii) In the special case where $|d|=1$, the two eigenvectors coincide, which can be expressed as

$$|\phi\rangle = \frac{1}{\sqrt{2}}\begin{pmatrix} 1 \\ \mathrm{i} \end{pmatrix}, \tag{13}$$

with the corresponding eigenvalue $E=0$. The points $d=\pm 1$ are usually referred to as the exceptional points.

Physically, the coalescence of eigenvectors at $d=\pm 1$ marks the transition between the $\mathcal{PT}$-symmetry unbroken phase and the $\mathcal{PT}$-symmetry broken phase [88, 89]. For $|d|<1$, the spectrum remains entirely real, and the system undergoes oscillatory evolution over time [90, 91]. However, for $|d|>1$, the eigenvalues become purely imaginary, leading to exponential growth or decay over time, characteristic of $\mathcal{PT}$-symmetry broken [92, 93]. Thus, the points $d=\pm 1$ signify the onset of this transition, where the system undergoes a qualitative change in its energy spectral properties [7]. Base on the preceding analysis of $E_\pm$, Fig. 2 is plotted to illustrate the dependence of the real part $\mathrm{Re}(E_\pm)$ and the imaginary part $\mathrm{Im}(E_\pm)$ on the parameter $|d|$. Noticing that $\bar{\delta}$ is always zero (i.e., $d\to\infty$) in the odd-parity case, the non-Hermitian spectral phase transition can only occur in the even-parity case by adjusting the frequency shift δ of the resonator.

3.2 Measurement of the energy spectrum

To firmly connect the theoretical spectrum in Figs. 2(a, b) to the proposed physical implementation, we further provide a numerical verification in which the complex eigenvalues $E_\pm$ of the non-Hermitian dynamical matrix $\mathcal{H}$ are retrieved from simulations of the full system dynamics governed by the complete Hamiltonian in Eq. (1). Concretely, we reconstruct the mode amplitudes from experimentally accessible quadratures of the resonator mode C,

$$X = a^\dagger + a, \qquad Y = \mathrm{i}\left(a^\dagger - a\right), \tag{14}$$

which can be obtained experimentally via homodyne detection or cavity state tomography [94–97]. The

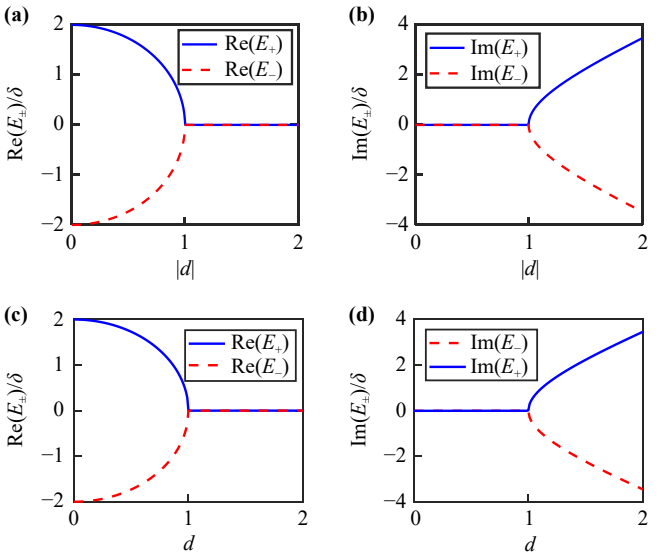

Fig. 2 Eigenvalue spectrum of the non-Hermitian dynamical matrix $\mathcal{H}$ across the same parameter sweep. **(a)** Real parts $\mathrm{Re}(E_\pm)/\delta$ and **(b)** imaginary parts $\mathrm{Im}(E_\pm)/\delta$ obtained from the theoretical analysis. **(c)** Reconstructed $\mathrm{Re}(E_\pm)/\delta$ and **(d)** reconstructed $\mathrm{Im}(E_\pm)/\delta$ retrieved from numerical simulations of the full system dynamics governed by the complete Hamiltonian in Eq. (1). In the simulations we use $\lambda_1 = 2\pi\times 50$ MHz, $\lambda_2 = \sqrt{1.5}\lambda_1$, $\Delta_1 = 2\pi\times 2.5$ GHz, and $\Delta_2 = 1.5\Delta_1$, and sweep the two-photon drive strength in the range $\xi\in[0,2\delta]$, with the short evolution time chosen as $\tau = 0.01$ μs.

complex amplitudes are reconstructed through

$$a = \frac{X+\mathrm{i}Y}{2}, \qquad a^\dagger = \frac{X-\mathrm{i}Y}{2}. \tag{15}$$

These quantities provide complete information about the mode amplitudes entering the effective non-Hermitian dynamics, and thus enable the reconstruction of the eigenvalues of $\mathcal{H}$.

To proceed, we define a vector of operator expected values as $|\psi(t)\rangle = [\langle a(t)\rangle, \langle a^\dagger(t)\rangle]^{\mathrm{T}}$. According to the Heisenberg equation of motion in Eq. (6), we obtain

$$\begin{aligned} \mathrm{i}\langle\dot{a}(t)\rangle &= 2\bar{\delta}\langle a(t)\rangle + 2\mathrm{i}\xi\langle a^\dagger(t)\rangle, \\ \mathrm{i}\langle\dot{a}^\dagger(t)\rangle &= 2\mathrm{i}\xi\langle a(t)\rangle - 2\bar{\delta}\langle a^\dagger(t)\rangle, \end{aligned} \tag{16}$$

which can further be rewritten by $\mathrm{i}\left|\dot{\psi}(t)\right\rangle = \mathcal{H}|\psi(t)\rangle$, i.e., the evolution of the vector also fulfills the Schrödinger-like equation governed by the dynamical matrix $\mathcal{H}$. Then, we introduce the right and left eigenvectors of $\mathcal{H}$,

$$\mathcal{H}|\phi_\mu\rangle = E_\mu|\phi_\mu\rangle, \qquad \langle\tilde{\phi}_\mu|\mathcal{H} = E_\mu\langle\tilde{\phi}_\mu|, \tag{17}$$

with $\mu=\pm$ and the biorthogonality condition

$$\langle\tilde{\phi}_\mu|\phi_\nu\rangle = \delta_{\mu\nu} \qquad (\mu,\nu=\pm). \tag{18}$$

Starting from a initial state $|\psi(0)\rangle$, the state $|\psi(\tau)\rangle$ at a short evolution time τ can be reconstructed from the

measured quadratures via Eq. (15). The complex eigenvalues are then retrieved from the overlap ratio

$$\begin{aligned}\mathrm{Re}(E_\pm) &= -\frac{1}{\tau}\arg\left[\frac{\langle\tilde{\phi}_\pm|\psi(\tau)\rangle}{\langle\tilde{\phi}_\pm|\psi(0)\rangle}\right],\\ \mathrm{Im}(E_\pm) &= \frac{1}{\tau}\ln\left|\frac{\langle\tilde{\phi}_\pm|\psi(\tau)\rangle}{\langle\tilde{\phi}_\pm|\psi(0)\rangle}\right|.\end{aligned} \tag{19}$$

A detailed derivation is provided in Appendix C.

In the numerical verification, we first calculate the density operator $\rho(\tau)$ of the system with the full Hamiltonian given by Eq. (1) in the Schrödinger picture. Subsequently, the expected values of the operators $X(\tau)$ and $Y(\tau)$ can be obtained through the relation

$$\langle X(\tau)\rangle = \mathrm{Tr}[\rho(\tau)X],\ \langle Y(\tau)\rangle = \mathrm{Tr}[\rho(\tau)Y]. \tag{20}$$

Using Eq. (15), the vector $|\psi(t)\rangle$ can be reconstructed as

$$|\psi(\tau)\rangle = \frac{1}{2}\begin{pmatrix}\mathrm{Tr}[\rho(\tau)X] + \mathrm{iTr}[\rho(\tau)Y]\\ \mathrm{Tr}[\rho(\tau)X] - \mathrm{iTr}[\rho(\tau)Y]\end{pmatrix}. \tag{21}$$

Based on the retrieval formulas in Eq. (19), one can obtain the energy spectra of the dynamical matrix $\mathcal{H}$. The resulting reconstructed spectra are plotted in Figs. 2(c, d), which quantitatively reproduce the analytical eigenvalues shown in Figs. 2(a, b) and clearly capture the same phase-transition signature. This demonstrates that the non-Hermitian spectral transition predicted for $\mathcal{H}$ is observable within the proposed physical model.

In the following, we exploit this parity-dependent spectral phase transition to map the qubit parity onto two sharply different photon-number dynamics of the auxiliary resonator (exponential growth versus bounded oscillations), enabling parity discrimination via a simple threshold measurement. More broadly, the parity-controlled transition between oscillatory and exponentially growing dynamics can be viewed as a simple instance of non-Hermitian mode control enabled by spectral phase transitions/exceptional points, which has attracted increasing attention in recent studies [58, 98].

4 Parity detection based on non-Hermitian spectral phase transition

The odd-parity state and the even-parity state are defined as

$$\begin{aligned}|\psi_{\mathrm{odd}}\rangle &= \beta_1|g,e\rangle_{1,2} + \beta_2|e,g\rangle_{1,2},\\ |\psi_{\mathrm{even}}\rangle &= \beta_3|g,g\rangle_{1,2} + \beta_4|e,e\rangle_{1,2},\end{aligned} \tag{22}$$

which correspond to the eigenvectors of the two-qubit parity operator $\mathcal{P}_2 = \sigma_{z,1}\otimes\sigma_{z,2}$ with eigenvalues -1 and $+1$, respectively. The normalization coefficients satisfy $|\beta_1|^2 + |\beta_2|^2 = 1$ and $|\beta_3|^2 + |\beta_4|^2 = 1$. Furthermore, the Pauli-Z operator for the qubit q_n is defined as $\sigma_{z,n} = |e\rangle_n\langle e| - |g\rangle_n\langle g|$.

Substituting $\bar{\delta} = 0$, the evolution of the operator in the Heisenberg picture follows

$$\mathrm{i}\dot{a} = 2\mathrm{i}\xi a^\dagger, \quad \mathrm{i}\dot{a}^\dagger = 2\mathrm{i}\xi a, \tag{23}$$

which can be rewritten as

$$\mathrm{i}\frac{\mathrm{d}}{\mathrm{d}t}\boldsymbol{v}(t) = \mathcal{H}_o\boldsymbol{v}(t), \tag{24}$$

with

$$\mathcal{H}_o = \begin{pmatrix}0 & 2\mathrm{i}\xi\\ 2\mathrm{i}\xi & 0\end{pmatrix} = 2\mathrm{i}\xi\mathcal{A}_o\sigma_z\mathcal{A}_o^{-1}. \tag{25}$$

Here, we define

$$\mathcal{A}_o = \frac{1}{\sqrt{2}}\begin{pmatrix}1 & 1\\ 1 & -1\end{pmatrix}. \tag{26}$$

The solution of Eq. (24) is given by

$$\boldsymbol{v}(t) = \mathcal{U}_o(t)\boldsymbol{v}(0) = \exp(-\mathrm{i}\mathcal{H}_o t)\boldsymbol{v}(0). \tag{27}$$

Using the result

$$\begin{aligned}\exp(-\mathrm{i}\mathcal{H}_o t) &= \mathcal{A}_o\exp(2\xi\sigma_z t)\mathcal{A}_o^{-1}\\ &= \begin{pmatrix}\cosh(2\xi t) & \sinh(2\xi t)\\ \sinh(2\xi t) & \cosh(2\xi t)\end{pmatrix},\end{aligned} \tag{28}$$

we derive

$$\begin{aligned}a(t) &= \cosh(2\xi t)a + \sinh(2\xi t)a^\dagger,\\ a^\dagger(t) &= \sinh(2\xi t)a + \cosh(2\xi t)a^\dagger,\end{aligned} \tag{29}$$

with $a(0) = a$ and $a^\dagger(0) = a^\dagger$. This gives rise to

$$\begin{aligned}a^\dagger(t)a(t) = {}& \cosh(4\xi t)a^\dagger a + \sinh(4\xi t)(a^{\dagger 2} + a^2)/2\\ &+ \sinh^2(2\xi t),\end{aligned} \tag{30}$$

which implies

$$\begin{aligned}N_o &= \langle a^\dagger(t)a(t)\rangle\\ &= \cosh(4\xi t)\langle a^\dagger a\rangle + \sinh(4\xi t)(\langle a^{\dagger 2}\rangle + \langle a^2\rangle)/2\\ &\quad + \sinh^2(2\xi t).\end{aligned} \tag{31}$$

If we initially prepare the resonator C in the coherence state $|\alpha\rangle_C$ with a real amplitude α, the average photon number is given by

$$\begin{aligned}N_o &= \cosh(4\xi t)\alpha^2 + \sinh(4\xi t)\alpha^2 + \sinh^2(2\xi t)\\ &= e^{4\xi t}\alpha^2 + \sinh^2(2\xi t).\end{aligned} \tag{32}$$

When the qubits are in the even-parity state $|g,g\rangle_{1,2}$ or $|e,e\rangle_{1,2}$, the dynamical matrix for the evolution of the operators a and $a^\dagger$ is given by

$$\mathcal{H}_e = \begin{pmatrix} \pm 2\delta & 2\mathrm{i}\xi \\ 2\mathrm{i}\xi & \mp 2\delta \end{pmatrix}, \tag{33}$$

by substituting $\bar{\delta} = \delta$ ($\bar{\delta} = -\delta$) for the case of $|g,g\rangle_{1,2}$ ($|e,e\rangle_{1,2}$). If we adjust the control parameter to make $|d| = |\xi/\delta| = \tanh 2\chi < 1$, according to the results in Section 3, the $\mathcal{PT}$-symmetry is unbroken and the imaginary parts $\mathrm{Im}(E_{\pm}^{e})$ of the eigenvalues of the dynamical matrix $\mathcal{H}_e$ are zero. The dynamical matrix $\mathcal{H}_e$ can be diagonalized as

$$\mathcal{H}_e = \mathcal{A}_e \bar{\mathcal{H}}_e \mathcal{A}_e^{-1}, \tag{34}$$

with

$$\begin{aligned} \overline{H}_e &= \begin{pmatrix} \pm 2\sqrt{\delta^2 - \xi^2} & 0 \\ 0 & \mp 2\sqrt{\delta^2 - \xi^2} \end{pmatrix}, \\ \mathcal{A}_e &= \begin{pmatrix} \cosh\chi & \sinh\chi \\ \pm\mathrm{i}\sinh\chi & \pm\mathrm{i}\cosh\chi \end{pmatrix}. \end{aligned} \tag{35}$$

Thus, the corresponding evolution operator can be calculated as

$$\begin{aligned} \mathcal{U}_e(t) =& \exp(-\mathrm{i}\mathcal{H}_e t) = \mathcal{A}_e \exp(-\mathrm{i}\bar{\mathcal{H}}_e t)\mathcal{A}_e^{-1} \\ =& \begin{pmatrix} \cos\theta \mp \mathrm{i}\sin\theta\cosh 2\chi & \sin\theta\sinh 2\chi \\ \sin\theta\sinh 2\chi & \cos\theta \pm \mathrm{i}\sin\theta\cosh 2\chi \end{pmatrix}, \end{aligned} \tag{36}$$

with $\theta = 2\sqrt{\delta^2 - \xi^2}t$. Using the result $\boldsymbol{v}(t) = \mathcal{U}_e(t)\boldsymbol{v}(0)$ we obtain

$$\begin{aligned} a(t) &= (\cos\theta \mp \mathrm{i}\sin\theta\cosh 2\chi)a + (\sin\theta\sinh 2\chi)a^{\dagger}, \\ a^{\dagger}(t) &= (\sin\theta\sinh 2\chi)a + (\cos\theta \pm \mathrm{i}\sin\theta\cosh 2\chi)a^{\dagger}, \end{aligned} \tag{37}$$

and

$$\begin{aligned} a^{\dagger}(t)a(t) =& (\cos^2\theta + \sin^2\theta\cosh 4\chi)a^{\dagger}a \\ &+ \sin 2\theta\sinh 2\chi(a^{\dagger 2} + a^2)/2 \\ &\pm \mathrm{i}\sin^2\theta\sin\theta\sinh 4\chi(a^{\dagger 2} - a^2)/2 \\ &+ \sin^2\theta\sinh 2\chi. \end{aligned} \tag{38}$$

When the resonator C is initially prepared in the same coherence state $|\alpha\rangle_C$ as that in the odd-parity case, the average photon number of the resonator C in this case reads

$$\begin{aligned} N_e =& \langle a^{\dagger}(t)a(t)\rangle \\ =& (\cos^2\theta + \sin^2\theta\cosh 4\chi)\alpha^2 + \alpha^2\sin 2\theta\sinh 2\chi \\ &+ \sin^2\theta\sinh 2\chi \\ =& (\cos^2\theta + \sin^2\theta\cosh 4\chi + \sin 2\theta\sinh 2\chi)\alpha^2 \\ &+ \sin^2\theta\sinh 2\chi. \end{aligned} \tag{39}$$

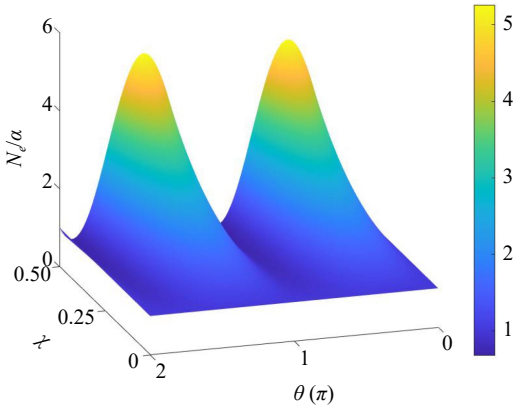

Fig. 3 Theoretical average photon number $N_e/|\alpha|^2$ as a function of θ and χ, evaluated from Eq. (39).

It can be seen that the average photon number of resonator C is the same for initial states $|g,g\rangle_{1,2}$ and $|e,e\rangle_{1,2}$. Therefore, the above analysis can be applied to an arbitrary even-parity state, as it can be expressed as a linear superposition of the states $|g,g\rangle_{1,2}$ and $|e,e\rangle_{1,2}$. We plot the average photon number N_e versus θ and χ in Fig. 3. As shown in the figure, for a fixed θ, a smaller χ corresponds to a lower maximum average photon number. When χ is fixed, the average photon number exhibits a periodic variation over time under a finite upper bound. Therefore, we can select a relatively small χ and a proper evolution time for a low photon number in the even-parity case. Comparing the variation of the photon number in the odd- and even-parity cases, it is possible to discriminate the parity of the qubits' state by measuring the photon number of the resonator.

As an example, we numerically simulate the average photon number of the resonator C on the density operator ρ_o (ρ_e) in the case of odd-parity (even-parity) of the system using the Liouville-von Neumann equation

$$\dot{\rho_k} = -\mathrm{i}[H, \rho_k], \tag{40}$$

with $k = o$, e, where H is the full Hamiltonian given in Eq. (1). The initial states of the qubits q_1 and q_2 are selected as

$$\begin{aligned} |\psi_o\rangle &= \frac{1}{\sqrt{2}}(|g,e\rangle_{q_1,q_2} + |e,g\rangle_{q_1,q_2}), \\ |\psi_e\rangle &= \frac{1}{\sqrt{2}}(|g,g\rangle_{q_1,q_2} + |e,e\rangle_{q_1,q_2}), \end{aligned} \tag{41}$$

in the odd-parity and the even-parity cases, respectively. The initial state of the resonator C is the coherence state with the complex amplitude $\alpha = \sqrt{2}$. The parameters are selected as $\lambda_1 = 2\pi \times 50$ MHz, $\lambda_2 = \sqrt{1.5}\lambda_1$, $\Delta_1 = 2\pi \times 2.5$ GHz, $\Delta_2 = 1.5\Delta_1$, and $\xi = 2.5$ MHz [99, 100], with the evolution time $\tau = 0.6\,\mu$s. We plot the average photon numbers N_o and N_e versus t in Fig. 4, respectively. It can be observed that when the qubits q_1 and q_2 are in

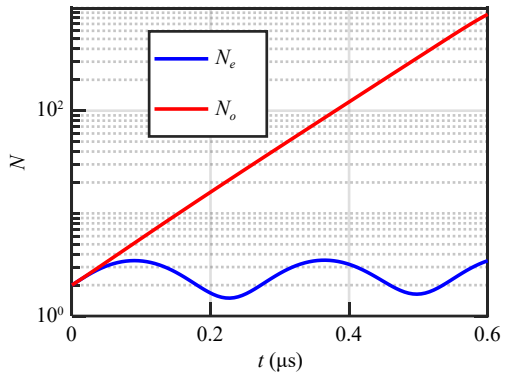

Fig. 4 Average photon numbers N_o and N_e versus t.

the odd-parity state, the average photon number of the resonator exhibits exponential growth, reaching $N_o = 868$ at $t = 0.6$ μs. In contrast, when the qubits are in the even-parity state, the average photon number undergoes periodic oscillations, with its maximum value approaching 3.5. The numerical simulation results closely align with the theoretical analysis. Therefore, we can distinguish the parity of qubits q_1 and q_2 by measuring the photon number in resonator C.

To achieve parity detection of qubits q_1 and q_2 by measuring the photon number in resonator C, we define a criterion for the parity detection: when the measured photon number satisfies $\mathcal{N} > m$ ($\mathcal{N} \leqslant m$), we recognize that the qubits q_1 and q_2 are in the odd-parity (even-parity) state. With such criterion, the error probabilities for the parity detection of an odd-parity state and an even-parity state can be calculated by

$$P_o = \mathrm{Tr}(\rho_o \mathcal{P}_{\mathcal{N}\leq m}),\ P_e = 1 - \mathrm{Tr}(\rho_e \mathcal{P}_{\mathcal{N}\leq m}), \tag{42}$$

with the projection operator

$$\mathcal{P}_{\mathcal{N}\leq m} = \sum_{j=0}^{m} |j\rangle_C\langle j|, \tag{43}$$

where $|j\rangle_C$ denotes the j-photon state of the resonator. To better distinguish the parity information of the qubits, we should select an appropriate m and operation time. Therefore, we consider the initial states of qubits q_1 and q_2 in the odd- and even-parity cases, as shown in Eq. (41). Using the same parameters as in Fig. 4, we plot the error probabilities P_o and P_e versus the evolution time t in Figs. 5(a) and (b), for different values of m. We consider relatively larger thresholds (e.g., $m = 6, 8, 10$) as conservative choices to suppress misclassification caused by residual photon-number fluctuations in the even-parity case. As shown in the figure, P_o decreases monotonically, while P_e exhibits oscillatory behavior. For the even-parity case, a relatively low error probability is observed in the time window of 0.5–0.52 μs. In contrast, within this time interval, the error probability P_o exceeds 0.01 for $m = 6$, 8, and 10, and only falls below 0.01 when $m = 4$. Therefore, $m = 4$ can be chosen as the photon-number threshold to distinguish the parity information of the qubits. For relatively small error probabilities P_o and P_e in the two cases, we select $t = 0.513$ μs as the operation time, at which the error probabilities are $P_o = 9.082 \times 10^{-3}$ and $P_e = 8.597 \times 10^{-3}$. At the selected operating time $t = 0.513$ μs, this choice places the threshold well above the oscillatory maxima of the even-parity photon-number dynamics, while remaining far below the exponentially increased photon number in the odd-parity case, thereby providing a clear physical separation between the two outcomes. The results indicate that by measuring the photon numbers in resonator C, it is possible to achieve a near-deterministic discrimination of the even- and odd-parity states of qubits q_1 and q_2 with an appropriate operation time.

From an experimental perspective, the achievable intracavity photon number may be limited by residual Kerr nonlinearity and by the finite dynamic range/saturation of the amplification chain at large output power. Moreover, the stability of the two-photon drive (setting ξ) and the calibration of dispersive shifts $\delta_n = \lambda_n^2/\Delta_n$ determine the operating ratio $|d| = |\xi/\bar{\delta}|$ and thus the contrast between oscillatory and amplifying dynamics. These constraints mainly affect the quantitative calibration of the photon-number separation, rather than the existence of the parity-dependent contrast; in practice, the operating time and threshold can be adjusted to keep a clear separation while avoiding unnecessarily large photon numbers.

In practice, the final step of our protocol only requires a threshold decision, i.e., whether the intracavity photon number satisfies $N \leq m$ or $N > m$, rather than full photon-number resolution. Such a threshold readout can be implemented in standard circuit-QED architectures in a quantum non-demolition (QND) manner, e.g., via dispersive coupling to an ancillary qubit and photon-number–selective interrogation (number splitting), or alternatively using microwave photon counters [101–103]. The main limitations include finite number splitting relative to the resonator linewidth, photon loss during the measurement window, and ancilla/readout noise, which may cause a small photon-number misassignment near the threshold. Notably, since the odd-parity case yields a much larger photon number at the chosen operating point, the readout requirement is primarily to separate low-photon even-parity outcomes from high-photon odd-parity outcomes, making the measurement less demanding than full number-resolved detection. Finally, our parity-controlled control of $\mathcal{PT}$-symmetry breaking connects naturally to recent experimental progress on manipulating exceptional points in effective anti-$\mathcal{PT}$-symmetric systems [104, 105].

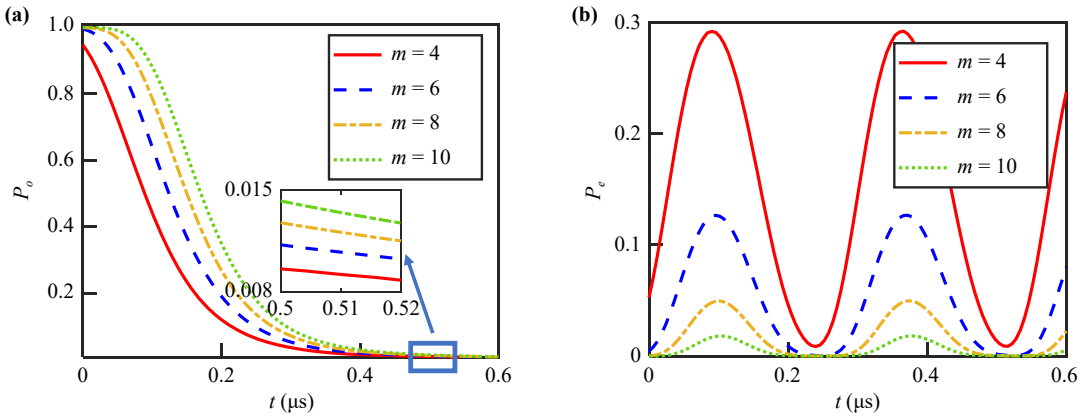

Fig. 5 **(a)** Error probabilities for the parity detection of an odd-parity state P_o versus t for different values of m. **(b)** Error probabilities for the parity detection of an even-parity state P_e versus t for different values of m.

5 Numerical simulation

In Section 4, we have demonstrated that the non-Hermitian phase transition in the spectrum of the dynamical matrix can be leveraged to achieve parity detection by measuring the photon number in the resonator. To assess the robustness of the parity detection, we analyze the error probabilities under the influence of various perturbation factors in this section. In the following discussion, we still adopt the parameters $\lambda_1 = 2\pi\times$ 50 MHz, $\lambda_2 = \sqrt{1.5}\lambda_1$, $\Delta_1 = 2\pi \times 2.5$ GHz, $\Delta_2 = 1.5\Delta_1$, and $\xi = 2.5$ MHz [99, 100], and an operation evolution time $\tau = 0.513$ μs. The corresponding odd-parity state and even-parity state in the system are still as shown in Eq. (41). Unless otherwise stated, the robustness analysis in this section is divided into three parts: (i) systematic errors are evaluated under unitary dynamics by evolving Eq. (40) with modified parameters, while (ii) decoherence effects are evaluated using the Lindblad master equation in Eq. (45), where we vary one decoherence channel at a time and set the other decoherence rates to zero; and (iii) we further examine the sensitivity of the protocol to the initial state of the resonator by the error-probability analysis for non-ideal initial states (e.g., a thermal state and a squeezed coherent state).

5.1 Influence of systematic errors

Due to imperfections of the instruments and the operations, there may exist systematic errors in the control parameters [106–109]. Here, the systematic errors may appear in the coupling strength λ_n $(n = 1, 2)$, the detuning Δ_n, and the amplitude ξ of the two-photon drive. Under the influence of systematic errors, these parameters are described as

$$\begin{aligned} &\lambda_1 \to (1+\eta_1)\lambda_1, \quad \lambda_2 \to (1+\eta_2)\lambda_2, \\ &\Delta_1 \to (1+\eta_3)\Delta_1, \quad \Delta_2 \to (1+\eta_4)\Delta_2, \\ &\xi \to (1+\eta_5)\xi, \end{aligned} \tag{44}$$

where η_l $(l = 1, 2, \cdots, 5)$ is the systematic error coefficient for the corresponding parameter.

The error probabilities P_o and P_e versus the systematic error coefficients η_l $(l = 1, 2, \cdots, 5)$ are plotted in Figs. 6(a) and (b), respectively. As shown in Fig. 6(a), the probability P_o exhibits insensitivity to systematic errors in coupling strength and detuning, with deviations not exceeding 2.6×10^{-4} across the considered error range. For the systematic error in the drive amplitude ξ, as indicated by Eq. (32), the drive amplitude ξ directly influences the photon number distribution in the resonator, leading to a decrease in the error probability as the drive amplitude increases. However, within the error coefficient range $\eta_5 \in [-0.05, 0.05]$, the error probability P_o remains below 1.011×10^{-2}. Therefore, the measurement of the odd-parity state demonstrates robustness against systematic errors in coupling strength, detuning, and amplitude.

As shown in Fig. 6(b), the probability P_e for measuring the even-parity state increases with the absolute value of the systematic error coefficient η_l. According to Eqs. (33)–(39) and Fig. 3, variations in coupling strength, detuning, and drive amplitude all influence the photon number variation within the resonator. Specifically, the drive amplitude influences the maximum average photon number achievable within a period, while the coupling strength and detuning primarily determine the variation period of the photon number. Consequently, from a fixed operation time, systematic errors in coupling strengths and detunings have a more significant impact on the error probability of even-parity state measurements, whereas the effect of drive-amplitude fluctuation is relatively minor. Because the deviation of the period makes the error probability P_e deviates from its local minimum. For $|\eta_l| \leqslant 0.05$, the error probability P_e remains below 4.439×10^{-2}. This indicates that the measurement of the even-parity state maintains a relatively high success probability despite the presence of systematic errors in the coupling strength, detuning, and drive

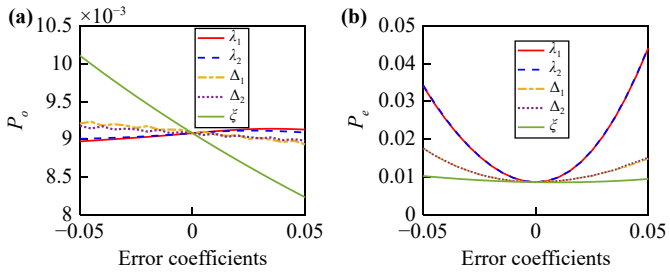

Fig. 6 **(a)** Error probability P_o versus the systematic error coefficients. **(b)** Error probability P_e versus the systematic error coefficients.

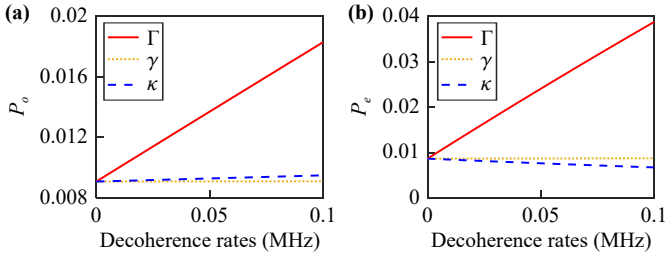

Fig. 7 **(a)** Error probability P_o versus the decoherence rates. **(b)** Error probability P_e versus the decoherence rates.

amplitude. If instrumental precision and operational accuracy are well maintained, keeping the error coefficient η_l within 0.01 ensures that the error probability remains below 9.867×10^{-3}.

5.2 Influence of decoherence

Decoherence is unavoidable in experimental implementations. The main sources of decoherence in the protocol include: (i) the spontaneous emission of the qubit q_n from the excited state $|e\rangle_n$ to the ground state $|g\rangle_n$, with the spontaneous emission rate of Γ_n; (ii) the dephasing of the qubit q_n on the excited state $|e\rangle_n$, with the dephasing rate γ_n; (iii) the decay of the resonator C, with the decay rate κ. Under the influence of these decoherence factors, the evolution of the system are governed by the master equation [110–113]

$$\begin{aligned}\dot{\rho_k} = & -\mathrm{i}[H, \rho_k] + \sum_{n=1}^{2} \Gamma_n \mathcal{L}[|g\rangle_n\langle e|]\rho_k \\ & + \sum_{n=1}^{2} \gamma_n \mathcal{L}[|e\rangle_n\langle e|]\rho_k + \kappa \mathcal{L}[a]\rho_k, \end{aligned} \tag{45}$$

with the Lindblad superoperator $\mathcal{L}[\mathcal{X}]\rho = \mathcal{X}\rho\mathcal{X}^\dagger - (\mathcal{X}^\dagger\mathcal{X}\rho + \rho\mathcal{X}^\dagger\mathcal{X})/2$ and $\mathcal{X} \in \{|g\rangle_n\langle e|,\ |e\rangle_n\langle e|,\ a\}$. For simplicity, we assume $\Gamma_1 = \Gamma_2 = \Gamma$ and $\gamma_1 = \gamma_2 = \gamma$ in the numerical simulations.

In Fig. 7, we plot the error probabilities P_o and P_e versus the decoherence rates, respectively. It is evident from the figure that the error probability for both even- and odd-parity cases remains largely unaffected by qubit dephasing. Within the dephasing rate range from 0 to 0.1 MHz [114, 115], the variation in error probabilities remains below 10^{-5}.

In the presence of cavity decay, the error probability P_o exhibits an increasing trend, while the error probability P_e shows a decreasing trend, and the overall deviation amplitude of the error probabilities are relatively small. It is worth noting that when the cavity decay rate $\kappa \leqslant 0.1$ MHz, the error probability P_o remains less than 10^{-2}.

In comparison, spontaneous emission leads to a relatively significant increase in the error probability for the both cases. This is because spontaneous emission of the qubits disrupts the parity information, thereby increasing the likelihood of measurement errors. For spontaneous emission rates up to $\Gamma = 0.1$ MHz, the error probabilities remain below $P_o \leqslant 1.830 \times 10^{-2}$ and $P_e \leqslant 3.882 \times 10^{-2}$. Considering an available parameter $\Gamma = 0.02$ MHz [116–118], the error probabilities for the odd- and even-parity cases are as low as 1.094×10^{-2} and 1.491×10^{-2}, respectively. According to the numerical results in this section, the protocol possess good robustness against the influence of decoherence.

Although Sections 5.1 and 5.2 quantify robustness mainly through the final misclassification probabilities P_o and P_e, these error probabilities are ultimately determined by how imperfections reshape the photon-number dynamics relative to the fixed threshold m. In our protocol, the parity information is mapped onto two distinct dynamical regimes of the auxiliary resonator: an amplifying (exponentially growing) photon-number evolution in the odd-parity sector versus a bounded oscillatory evolution in the even-parity sector. Systematic imperfections in λ_n, Δ_n, and ξ primarily act by renormalizing the effective dispersive shifts $\delta_n = \lambda_n^2/\Delta_n$ and the control ratio $|d| = |\xi/\bar{\delta}|$. In the even-parity sector, this renormalization mainly shifts the oscillation frequency/phase of the bounded trajectory and therefore displaces the time locations of the local minima of $P_e(t)$. In the odd-parity sector, it mainly modifies the effective amplification rate, which determines how rapidly the photon-number distribution moves above the fixed threshold. Decoherence channels included in our model act through distinct physical mechanisms on this threshold separation. Cavity decay mainly suppresses the buildup of large photon number, reducing the odd-parity amplification contrast while also tending to keep the even-parity population low. Qubit dephasing typically has a weaker influence here because the discrimination relies on parity-conditioned frequency shifts rather than preserving a specific relative phase within a given parity sector. In contrast, qubit relaxation can induce transitions between parity sectors during the evolution window, which directly increases the overlap between the even/odd

photon-number distributions and thus leads to the most noticeable increase in both P_o and P_e. Importantly, even when imperfections shift the transient photon-number trajectories, the protocol remains operational because one can re-optimize the operating time (and, if desired, the threshold) to recover a time window where both $P_o(t)$ and $P_e(t)$ are simultaneously small.

5.3 Parity detection using different initial state of the resonator

In the preceding analysis, the resonator is assumed to be initialized in a coherent state. To verify that the protocol is not restricted to the coherent-state initialization, we further examine the parity detection by the numerical evaluation of the time-dependent error probabilities $P_o(t)$ and $P_e(t)$ using two different initial states: a thermal state and a squeezed coherent state.

First, we take the resonator to start from a thermal state

$$\rho_{\rm th} = \sum_{n=0}^{\infty} p_n |n\rangle\langle n|, \quad p_n = \frac{\bar{n}_{\rm th}^{\,n}}{(1+\bar{n}_{\rm th})^{n+1}}, \tag{46}$$

where $\bar{n}_{\rm th}$ is the mean thermal photon number. In Fig. 8(a), we choose $\bar{n}_{\rm th} = 0.2$. For each evolution time t, we evolve the initial state $\rho_{o/e}(0) = |\psi_{o/e}\rangle\langle\psi_{o/e}| \otimes \rho_{\rm th}$ under the same dynamical equation as in Eq. (40) and compute $P_o(t)$ and $P_e(t)$ using the same photon-number threshold m.

We also consider a squeezed coherent state

$$\rho_{\rm sq} = |\alpha,\zeta\rangle\langle\alpha,\zeta|, \quad |\alpha,\zeta\rangle = S(\zeta)D(\alpha)|0\rangle, \tag{47}$$

where $D(\alpha) = \exp(\alpha a^\dagger - \alpha^* a)$ is the displacement operator and $S(\zeta) = \exp\left[\frac{1}{2}(\zeta^* a^2 - \zeta a^{\dagger 2})\right]$ is the squeezing operator with $\zeta = r e^{i\phi}$. In Fig. 8(b), we fix the coherent amplitude to $\alpha = \sqrt{2}$ and choose $r = 0.4$ with $\phi = 0$. The corresponding initial states are $\rho_{o/e}(0) = |\psi_{o/e}\rangle\langle\psi_{o/e}| \otimes \rho_{\rm sq}$, and we evaluate the same error probabilities $P_o(t)$ and $P_e(t)$ as functions of t.

The numerical results are summarized in Fig. 8. In both panels, the photon-number dynamics still provides a clear separation between the two parity outcomes even for non-ideal resonator initial states, and low misclassification probabilities can be achieved by choosing an appropriate operating time. For a fair comparison, the value of the photon number threshold m remains the same as before. However, since the initial photon-number statistics modifies the transient evolution, the optimal operating time window is shifted compared with the coherent initialization. Specifically, for the thermal initial state in Fig. 8(a), we identify a time window $t \simeq 1.17$–1.20 μs where both $P_o(t)$ and $P_e(t)$ remain below 0.01. For the squeezed coherent initial state in Fig. 8(b), we find a broad low-error window $t \simeq 0.546$–0.588 μs with $P_o(t), P_e(t) < 0.01$. These results confirm that the proposed parity detection remains effective beyond a coherent-state initialization, while in practice the operating time can be re-optimized (with the same threshold) to maintain low error probabilities.

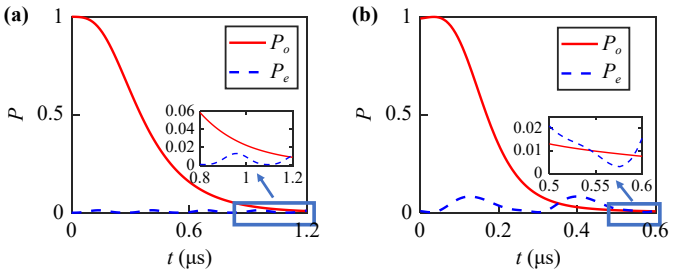

Fig. 8 Error probabilities $P_o(t)$ and $P_e(t)$ versus the evolution time t for different initial states of the resonator. **(a)** Thermal initial state $\rho_{\rm th}$ with mean photon number $\bar{n}_{\rm th} = 0.2$. **(b)** Squeezed coherent initial state $\rho_{\rm sq} = |\alpha,\zeta\rangle\langle\alpha,\zeta|$ with $\alpha = \sqrt{2}$ and squeezing parameter $\zeta = re^{i\phi}$ chosen as $r = 0.4$ and $\phi = 0$.

6 Conclusion

In summary, we have proposed an effective protocol for measuring the parity of a bipartite system based on non-Hermitian spectral phase transitions. The physical model contains two superconducting qubits as information carriers and a superconducting resonator as an auxiliary element. The qubits are simultaneously coupled to the resonator, which is driven by a two-photon drive. Under appropriate parameter settings, we derive an effective Hamiltonian for the system, which depends on the parity of the qubit states. The derived effective Hamiltonian indicates that a frequency shift of the resonator occurs when the qubits are in an even-parity state. By tuning the parity-dependent frequency shift, we show that, in the Heisenberg picture, the dynamical matrix, describing the evolution of the annihilation and creation operators of the resonator, undergoes a non-Hermitian spectral phase transition, where the spectrum turns from purely imaginary to purely real. This spectral phase transition results in distinct behaviors of photon number variations in the even- and odd-parity cases. Specifically, the purely imaginary spectrum results in exponential growth of the photon number in the odd-parity case, while the purely real spectrum leads to bounded oscillations of the photon number in the even-parity case. This enables the discrimination of the qubit state parities through photon number measurements. Numerical simulations further demonstrate that the protocol is robust against decoherence and parameter imperfections. Therefore, the protocol may provide a promising application of non-Hermitian dynamics under currently available technology.

Although we have focused on a two-qubit setting, the

underlying idea can be extended to a multi-qubit architecture. In the dispersive regime, each qubit contributes an ac-Stark shift to the auxiliary resonator; by suitably engineering and calibrating the dispersive couplings, the global parity information can be mapped onto two distinct dynamical behaviors of the resonator (bounded versus amplifying), enabling a multi-qubit parity readout using the same threshold-based photon-number decision. Practical considerations for scaling include the calibration overhead, the required readout dynamic range, and mitigating crosstalk and decoherence during the measurement window.

Declarations The authors declare that they have no competing interests and there are no conflicts.

Acknowledgements Y.-H. K. was supported by the National Key Research and Development Program of China (No. 2024YFA1408900) and the National Natural Science Foundation of China (No. U21A20436). Y.-H.C. was supported by the National Natural Science Foundation of China (Nos. 12304390 and 12574386), the Fujian 100 Talents Program, and the Fujian Minjiang Scholar Program. Y. X. was supported by the National Natural Science Foundation of China (No. 62471143) and the Key Program of National Natural Science Foundation of Fujian Province (No. 2024J02008).

Appendix A: Derivation of the effective Hamiltonian in Eq. (2)

For reproducibility, we provide a more explicit second-order derivation from the full Hamiltonian Eq. (1). We first separate the Hamiltonian as

$$H(t) = H_d + \sum_j \left(h_j^\dagger e^{i\omega_j t} + h_j e^{-i\omega_j t} \right), \tag{A1}$$

where $H_d = i\xi(a^{\dagger 2} - a^2)$ is the two-photon drive, and the oscillating terms originate from the qubit–resonator coupling. Following Ref. [80], under the condition $\omega_j \gg \|h_j\|$, the effective Hamiltonian up to second order can be written as

$$H_{\text{eff}} = H_d + \sum_{j,j'} \frac{1}{2} \left(\frac{1}{\omega_j} + \frac{1}{\omega_{j'}} \right) \left[h_j^\dagger, h_{j'} \right] e^{i(\omega_j - \omega_{j'})t}, \tag{A2}$$

where the secular (time-independent) contributions come from the $j = j'$ terms, while the $j \neq j'$ terms oscillate at frequency $|\omega_j - \omega_{j'}|$.

For Eq. (1), we choose

$$h_1 = \lambda_1 a |e\rangle_1\langle g|, \quad h_2 = \lambda_2 a |e\rangle_2\langle g|,$$
$$\omega_1 = \Delta_1, \quad \omega_2 = \Delta_2. \tag{A3}$$

The $j = j'$ commutators give the dispersive contributions:

$$\begin{aligned} \left[h_n^\dagger, h_n \right] &= \lambda_n^2 \left(a^\dagger a |g\rangle_n\langle g| - a a^\dagger |e\rangle_n\langle e| \right) \\ &= \lambda_n^2 \left(a^\dagger a |g\rangle_n\langle g| - a^\dagger a |e\rangle_n\langle e| - |e\rangle_n\langle e| \right), \end{aligned} \tag{A4}$$

where we used $aa^\dagger = a^\dagger a + 1$. Substituting this into Eq. (A2) yields

$$H_{\text{eff}} = i\xi(a^{\dagger 2} - a^2) + \sum_{n=1}^{2} \frac{\lambda_n^2}{\Delta_n} (a^\dagger a |g\rangle_n\langle g| - a^\dagger a |e\rangle_n\langle e| - |e\rangle_n\langle e|), \tag{A5}$$

which is Eq. (2) in the main text.

We now clarify the origin of the additional condition on $|\Delta_2 - \Delta_1|$. The $j \neq j'$ commutators in Eq. (A2) generate cross terms oscillating at frequency $|\Delta_2 - \Delta_1|$. Their characteristic prefactor is of order

$$J \sim \frac{\lambda_1 \lambda_2}{2} \left(\frac{1}{\Delta_1} + \frac{1}{\Delta_2} \right). \tag{A6}$$

When

$$|\Delta_2 - \Delta_1| \gg J, \tag{A7}$$

these fast-rotating cross terms average out and can be neglected (a rotating-wave/large-detuning argument). Therefore, the explicit time dependence in Eq. (1) is removed at second order and one obtains the time-independent effective Hamiltonian Eq. (A5).

Finally, to obtain Eq. (3), we define $\delta_n = \lambda_n^2/\Delta_n$ and the two-qubit basis

$$\begin{aligned} &|g,g\rangle_{1,2} \equiv |g\rangle_1 \otimes |g\rangle_2, \quad |e,g\rangle_{1,2} \equiv |e\rangle_1 \otimes |g\rangle_2, \\ &|g,e\rangle_{1,2} \equiv |g\rangle_1 \otimes |e\rangle_2, \quad |e,e\rangle_{1,2} \equiv |e\rangle_1 \otimes |e\rangle_2. \end{aligned} \tag{A8}$$

The coefficient of $a^\dagger a$ in Eq. (2) depends on the two-qubit state: it is $(\delta_1 + \delta_2)$ for $|g,g\rangle_{1,2}$, $-(\delta_1 + \delta_2)$ for $|e,e\rangle_{1,2}$, and $(\delta_2 - \delta_1)$ $[(\delta_1 - \delta_2)]$ for $|e,g\rangle_{1,2}$ $[|g,e\rangle_{1,2}]$. By choosing $\delta_1 = \delta_2 \equiv \delta$, the dispersive shift cancels in the odd-parity subspace while adding in the even-parity subspace, which leads directly to Eq. (3).

Appendix B: Equivalence between different phases of the two-photon drive

In this appendix, we prove that the non-Hermitian spectral phase transition of the Heisenberg-picture dynamical matrix, as well as the location of the exceptional point, is independent of the pump phase of the two-photon (squeezing) drive.

A general two-photon squeezing drive can be written as

$$H_{\text{sqz}}(\phi) = \xi \left(e^{i\phi} a^{\dagger 2} + e^{-i\phi} a^2 \right), \tag{B1}$$

where ϕ is the pump phase. Two special cases are:

$$\phi = 0: \quad H_{\mathrm{sqz}} = \xi(a^{\dagger 2} + a^2), \tag{B2}$$

$$\phi = \frac{\pi}{2}: \quad H_{\mathrm{sqz}} = \mathrm{i}\xi(a^{\dagger 2} - a^2), \tag{B3}$$

where Eq. (B3) is exactly the form used in the main text (with the same prefactor ξ).

Including the parity-dependent frequency shift, the reduced Hamiltonian becomes

$$\bar{H}(\phi) = \xi\left(\mathrm{e}^{\mathrm{i}\phi}a^{\dagger 2} + \mathrm{e}^{-\mathrm{i}\phi}a^2\right) + 2\bar{\delta}\,a^\dagger a. \tag{B4}$$

Using the Heisenberg equation $\dot{O} = i[\bar{H}(\phi), O]$, we obtain

$$\mathrm{i}\dot{a} = 2\bar{\delta}\,a + 2\xi\mathrm{e}^{\mathrm{i}\phi}a^\dagger, \tag{B5}$$

$$\mathrm{i}\dot{a}^\dagger = -2\xi\mathrm{e}^{-\mathrm{i}\phi}a - 2\bar{\delta}\,a^\dagger. \tag{B6}$$

Defining the operator vector $\boldsymbol{v}(t) = [a(t),\, a^\dagger(t)]^{\mathrm{T}}$, Eqs. (B5)–(B6) can be written as

$$\mathrm{i}\frac{\mathrm{d}}{\mathrm{d}t}\boldsymbol{v}(t) = \mathcal{H}(\phi)\boldsymbol{v}(t), \tag{B7}$$

with the dynamical matrix

$$\mathcal{H}(\phi) = \begin{pmatrix} 2\bar{\delta} & 2\xi\mathrm{e}^{\mathrm{i}\phi} \\ -2\xi\mathrm{e}^{-\mathrm{i}\phi} & -2\bar{\delta} \end{pmatrix}. \tag{B8}$$

The eigenvalues of $\mathcal{H}(\phi)$ are readily obtained as

$$E_\pm = \pm 2\sqrt{\bar{\delta}^{\,2} - \xi^2}, \tag{B9}$$

which are independent of ϕ. Therefore, the spectral phase transition (exceptional point) occurs at

$$|\bar{\delta}| = |\xi|, \tag{B10}$$

identical to the condition $|d| = |\xi/\bar{\delta}| = 1$ used in the main text. When $|\bar{\delta}| > |\xi|$, $E_\pm$ are real and the dynamics is oscillatory, whereas for $|\bar{\delta}| < |\xi|$, $E_\pm$ become purely imaginary and the dynamics exhibits exponential amplification/attenuation. This directly leads to the bounded versus exponentially growing photon-number behaviors exploited for parity discrimination.

Appendix C: Reconstruction of the non-Hermitian spectrum

In this appendix, we provide the derivation of the expressions used to retrieve the complex eigenvalues of the non-Hermitian dynamical matrix $\mathcal{H}$ from time-domain data.

For a non-Hermitian matrix $\mathcal{H}$, the right and left eigenvectors are defined by

$$\mathcal{H}|\phi_\mu\rangle = E_\mu|\phi_\mu\rangle, \qquad \langle\tilde{\phi}_\mu|\,\mathcal{H} = E_\mu\langle\tilde{\phi}_\mu|, \tag{C1}$$

with $\mu = \pm$. The left eigenvectors are not given by Hermitian conjugation of the right ones. Instead, they can be chosen to satisfy the biorthogonality condition

$$\langle\tilde{\phi}_\mu|\phi_\nu\rangle = \delta_{\mu\nu}. \tag{C2}$$

We consider the linear dynamics generated by $\mathcal{H}$,

$$|\psi(t)\rangle = \mathrm{e}^{-\mathrm{i}\mathcal{H}t}|\psi(0)\rangle, \tag{C3}$$

where $|\psi(0)\rangle$ is a known initial state. At any time t, the state can be expanded in the basis of right eigenvectors,

$$|\psi(t)\rangle = \sum_{\mu=\pm} c_\mu(t)\,|\phi_\mu\rangle. \tag{C4}$$

Projecting onto the left eigenvectors yields the expansion coefficients

$$c_\mu(t) = \langle\tilde{\phi}_\mu|\psi(t)\rangle. \tag{C5}$$

Using Eqs. (C1)–(C3), one obtains

$$c_\mu(t) = \langle\tilde{\phi}_\mu|\mathrm{e}^{-\mathrm{i}\mathcal{H}t}|\psi(0)\rangle = \mathrm{e}^{-\mathrm{i}E_\mu t}\,\langle\tilde{\phi}_\mu|\psi(0)\rangle. \tag{C6}$$

Taking the ratio of the coefficients at $t = \tau$ and $t = 0$ gives

$$\frac{c_\mu(\tau)}{c_\mu(0)} = \frac{\langle\tilde{\phi}_\mu|\psi(\tau)\rangle}{\langle\tilde{\phi}_\mu|\psi(0)\rangle} = \mathrm{e}^{-\mathrm{i}E_\mu\tau}. \tag{C7}$$

Therefore,

$$E_\mu = \frac{\mathrm{i}}{\tau}\ln\left[\frac{\langle\tilde{\phi}_\mu|\psi(\tau)\rangle}{\langle\tilde{\phi}_\mu|\psi(0)\rangle}\right], \tag{C8}$$

where $\ln$ denotes the complex logarithm. Writing $\ln z = \ln|z| + \mathrm{i}\arg(z)$ with $z_\mu = \langle\tilde{\phi}_\mu|\psi(\tau)\rangle/\langle\tilde{\phi}_\mu|\psi(0)\rangle$, we obtain

$$E_\mu = -\frac{1}{\tau}\arg(z_\mu) + \frac{\mathrm{i}}{\tau}\ln|z_\mu|. \tag{C9}$$

Separating the real and imaginary parts yields the retrieval formulas used in the main text:

$$\mathrm{Re}(E_\mu) = -\frac{1}{\tau}\arg\left[\frac{\langle\tilde{\phi}_\mu|\psi(\tau)\rangle}{\langle\tilde{\phi}_\mu|\psi(0)\rangle}\right], \tag{C10}$$

$$\mathrm{Im}(E_\mu) = \frac{1}{\tau}\ln\left|\frac{\langle\tilde{\phi}_\mu|\psi(\tau)\rangle}{\langle\tilde{\phi}_\mu|\psi(0)\rangle}\right|. \tag{C11}$$

References

1. F. Quijandría, U. Naether, S. K. Ozdemir, F. Nori, and D. Zueco, *PT*-symmetric circuit QED, *Phys. Rev. A* 97(5), 053846 (2018)
2. C. R. Leefmans, M. Parto, J. Williams, G. H. Y. Li, A.

Dutt, F. Nori, and A. Marandi, Topological temporally mode-locked laser, *Nat. Phys.* 20(5), 852 (2024)
3. I. I. Arkhipov, F. Minganti, A. Miranowicz, and F. Nori, Generating high-order quantum exceptional points in synthetic dimensions, *Phys. Rev. A* 104(1), 012205 (2021)
4. K. Shi, L. Qiao, Z. Zheng, and W. Zhang, Floquet topological phases and skin effects in periodically driven non-Hermitian systems, *Phys. Rev. A* 110(2), 022222 (2024)
5. Z. H. Yuan, Z. Geng, Y. J. Chen, Y. Xia, Y. Y. Jiang, and J. Song, Nanoparticle-mediated controlled entanglement based on non-Hermitian coupling, *Phys. Rev. A* 110(2), 023732 (2024)
6. G. Q. Zhang, Z. Chen, W. Xiong, C. H. Lam, and J. Q. You, Parity-symmetry-breaking quantum phase transition via parametric drive in a cavity magnonic system, *Phys. Rev. B* 104(6), 064423 (2021)
7. R. El-Ganainy, K. G. Makris, M. Khajavikhan, Z. H. Musslimani, S. Rotter, and D. N. Christodoulides, Non-Hermitian physics and *PT* symmetry, *Nat. Phys.* 14(1), 11 (2018)
8. W. Chen, M. Abbasi, Y. N. Joglekar, and K. W. Murch, Quantum jumps in the non-Hermitian dynamics of a superconducting qubit, *Phys. Rev. Lett.* 127(14), 140504 (2021)
9. G. Q. Zhang, Z. Chen, D. Xu, N. Shammah, M. Liao, T. F. Li, L. Tong, S. Y. Zhu, F. Nori, and J. Q. You, Exceptional point and cross-relaxation effect in a hybrid quantum system, *PRX Quantum* 2(2), 020307 (2021)
10. E. J. Bergholtz, J. C. Budich, and F. K. Kunst, Exceptional topology of non-Hermitian systems, *Rev. Mod. Phys.* 93(1), 015005 (2021)
11. H. Wang, B. Xie, and W. Ren, Finite-size-induced non-Hermitian phase transitions in real space, *Sci. China Phys. Mech. Astron.* 67(11), 117011 (2024)
12. X. X. Zhang and N. Nagaosa, Topological spin textures in electronic non-Hermitian systems, *Sci. Bull. (Beijing)* 69(3), 325 (2024)
13. W. Chen, M. Abbasi, B. Ha, S. Erdamar, Y. N. Joglekar, and K. W. Murch, Decoherence-induced exceptional points in a dissipative superconducting qubit, *Phys. Rev. Lett.* 128(11), 110402 (2022)
14. P. R. Han, F. Wu, X. J. Huang, H. Z. Wu, C. L. Zou, W. Yi, M. Zhang, H. Li, K. Xu, D. Zheng, H. Fan, J. Wen, Z. B. Yang, and S. B. Zheng, Exceptional entanglement phenomena: Non-Hermiticity meeting nonclassicality, *Phys. Rev. Lett.* 131(26), 260201 (2023)
15. P. R. Han, W. Ning, X. J. Huang, R. H. Zheng, S. B. Yang, F. Wu, Z. B. Yang, Q. P. Su, C. P. Yang, and S. B. Zheng, Measuring topological invariants for high-erorder exceptional points in quantum three-mode systems, *Nat. Commun.* 15(1), 10293 (2024)
16. Ş. K. Özdemir, S. Rotter, F. Nori, and L. Yang, Parity–time symmetry and exceptional points in photonics, *Nat. Mater.* 18(8), 783 (2019)
17. M. Parto, C. Leefmans, J. Williams, F. Nori, and A. Marandi, Non-Abelian effects in dissipative photonic topological lattices, *Nat. Commun.* 14(1), 1440 (2023)
18. Q. C. Wu, J. L. Zhao, Y. L. Fang, Y. Zhang, D. X. Chen, C. P. Yang, and F. Nori, Extension of Noether's theorem in *PT*-symmetry systems and its experimental demonstration in an optical setup, *Sci. China Phys. Mech. Astron.* 66(4), 240312 (2023)
19. P. A. McClarty and J. G. Rau, Non-Hermitian topology of spontaneous magnon decay, *Phys. Rev. B* 100(10), 100405 (2019)
20. R. Wen, C. L. Zou, X. Zhu, P. Chen, Z. Y. Ou, J. F. Chen, and W. Zhang, Non-Hermitian magnon–photon interference in an atomic ensemble, *Phys. Rev. Lett.* 122(25), 253602 (2019)
21. J. Qian, J. Li, S. Y. Zhu, J. Q. You, and Y. P. Wang, Probing *PT*-symmetry breaking of non-Hermitian topological photonic states via strong photon–magnon coupling, *Phys. Rev. Lett.* 132(15), 156901 (2024)
22. D. Zhang, X. Q. Luo, Y. P. Wang, T. F. Li, and J. Q. You, Observation of the exceptional point in cavity magnon-polaritons, *Nat. Commun.* 8(1), 1368 (2017)
23. W. W. Jin, J. Liu, X. Wang, Y. R. Zhang, X. Huang, X. Wei, W. Ju, Z. Yang, T. Liu, and F. Nori, Anderson delocalization in strongly coupled disordered non-Hermitian chains, *Phys. Rev. Lett.* 135(7), 076602 (2025)
24. C. Leefmans, A. Dutt, J. Williams, L. Yuan, M. Parto, F. Nori, S. Fan, and A. Marandi, Topological dissipation in a time-multiplexed photonic resonator network, *Nat. Phys.* 18(4), 442 (2022)
25. C. Y. Ju, A. Miranowicz, F. Minganti, C. T. Chan, G. Y. Chen, and F. Nori, Einstein's quantum elevator: Hermitization of non-Hermitian Hamiltonians via a generalized vielbein formalism, *Phys. Rev. Res.* 4(2), 023070 (2022)
26. J. X. Han, J. L. Wu, Z. H. Yuan, Y. Xia, Y. Y. Jiang, and J. Song, Fast topological pumping for the generation of large-scale Greenberger–Horne–Zeilinger states in a superconducting circuit, *Front. Phys. (Beijing)* 17(6), 62504 (2022)
27. M. Naghiloo, M. Abbasi, Y. N. Joglekar, and K. W. Murch, Quantum state tomography across the exceptional point in a single dissipative qubit, *Nat. Phys.* 15(12), 1232 (2019)
28. R. Uzdin, A. Mailybaev, and N. Moiseyev, On the observability and asymmetry of adiabatic state flips generated by exceptional points, *J. Phys. A Math. Theor.* 44(43), 435302 (2011)
29. J. Doppler, A. A. Mailybaev, J. Bohm, U. Kuhl, A. Girschik, F. Libisch, T. J. Milburn, P. Rabl, N. Moiseyev, and S. Rotter, Dynamically encircling an exceptional point for asymmetric mode switching, *Nature* 537(7618), 76 (2016)
30. I. I. Arkhipov, F. Minganti, A. Miranowicz, Ş. K. Özdemir, and F. Nori, Restoring adiabatic state transfer in time-modulated non-Hermitian systems, *Phys. Rev. Lett.* 133(11), 113802 (2024)
31. J. Wingenbach, S. Schumacher, and X. Ma, Manipulating spectral topology and exceptional points by nonlinearity in non-Hermitian polariton systems, *Phys. Rev. Res.* 6(1), 013148 (2024)
32. H. K. Lau and A. A. Clerk, Fundamental limits and non-reciprocal approaches in non-Hermitian quantum sensing, *Nat. Commun.* 9(1), 4320 (2018)

33. J. L. Wu, Y. Wang, J. X. Han, S. L. Su, Y. Xia, Y. Jiang, and J. Song, Unselective ground-state blockade of Rydberg atoms for implementing quantum gates, *Front. Phys. (Beijing)* 17(2), 22501 (2022)
34. H. Hodaei, A. U. Hassan, S. Wittek, H. Garcia-Gracia, R. El-Ganainy, D. N. Christodoulides, and M. Khajavikhan, Enhanced sensitivity at higher-order exceptional points, *Nature* 548(7666), 187 (2017)
35. W. Chen, Ş. Kaya Özdemir, G. Zhao, J. Wiersig, and L. Yang, Exceptional points enhance sensing in an optical microcavity, *Nature* 548(7666), 192 (2017)
36. X. Wang and G. Ma, Experimental measurement of non-Hermitian left eigenvectors, *Front. Phys. (Beijing)* 20(5), 054202 (2025)
37. M. V. Berry and R. Uzdin, Slow non-Hermitian cycling: exact solutions and the stokes phenomenon, *J. Phys. A Math. Theor.* 44(43), 435303 (2011)
38. E. M. Graefe, A. A. Mailybaev, and N. Moiseyev, Breakdown of adiabatic transfer of light in waveguides in the presence of absorption, *Phys. Rev. A* 88(3), 033842 (2013)
39. S. Ibáñez and J. G. Muga, Adiabaticity condition for non-Hermitian Hamiltonians, *Phys. Rev. A* 89(3), 033403 (2014)
40. T. J. Milburn, J. Doppler, C. A. Holmes, S. Portolan, S. Rotter, and P. Rabl, General description of quasi-adiabatic dynamical phenomena near exceptional points, *Phys. Rev. A* 92(5), 052124 (2015)
41. H. Xu, D. Mason, L. Jiang, and J. G. E. Harris, Topological energy transfer in an optomechanical system with exceptional points, *Nature* 537(7618), 80 (2016)
42. X. L. Zhang, S. Wang, B. Hou, and C. T. Chan, Dynamically encircling exceptional points: In situ control of encircling loops and the role of the starting point, *Phys. Rev. X* 8(2), 021066 (2018)
43. J. Höller, N. Read, and J. G. E. Harris, Non-Hermitian adiabatic transport in spaces of exceptional points, *Phys. Rev. A* 102(3), 032216 (2020)
44. S. Zhang, Y. Hu, G. Lin, Y. Niu, K. Xia, J. Gong, and S. Gong, Thermal-motion-induced non-reciprocal quantum optical system, *Nat. Photonics* 12(12), 744 (2018)
45. X. X. Hu, Z. B. Wang, P. Zhang, G. J. Chen, Y. L. Zhang, G. Li, X. B. Zou, T. Zhang, H. X. Tang, C. H. Dong, G. C. Guo, and C. L. Zou, Noiseless photonic non-reciprocity via optically-induced magnetization, *Nat. Commun.* 12(1), 2389 (2021)
46. Q. Lin, W. Yi, and P. Xue, Manipulating directional flow in a two-dimensional photonic quantum walk under a synthetic magnetic field, *Nat. Commun.* 14(1), 6283 (2023)
47. Y. P. Wu, G. Q. Zhang, C. X. Zhang, J. Xu, and D. W. Zhang, Interplay of nonreciprocity and nonlinearity on mean-field energy and dynamics of a Bose–Einstein condensate in a double-well potential, *Front. Phys. (Beijing)* 17(4), 42503 (2022)
48. X. Zhang, T. Sun-Huo, and X. Zhang, Symmetryguided nonreciprocal transport in non-Hermitian scattering systems: Parity–flux reversal effects, *Front. Phys. (Beijing)* 21(4), 042203 (2026)
49. K. V. Kepesidis, T. J. Milburn, J. Huber, K. G. Makris, S. Rotter, and P. Rabl, *PT*-symmetry breaking in the steady state of microscopic gain–loss systems, *New J. Phys.* 18(9), 095003 (2016)
50. H. Jing, Ş. K. Özdemir, H. Lü, and F. Nori, High-order exceptional points in optomechanics, *Sci. Rep.* 7(1), 3386 (2017)
51. G. Q. Zhang and J. Q. You, Higher-order exceptional point in a cavity magnonics system, *Phys. Rev. B* 99(5), 054404 (2019)
52. W. Nie, T. Shi, Y. X. Liu, and F. Nori, Non-Hermitian waveguide cavity QED with tunable atomic mirrors, *Phys. Rev. Lett.* 131(10), 103602 (2023)
53. Z. H. Yuan, Y. J. Chen, J. X. Han, J. L. Wu, W. Q. Li, Y. Xia, Y. Y. Jiang, and J. Song, Periodic photon–magnon blockade in an optomagnonic system with chiral exceptional points, *Phys. Rev. B* 108(13), 134409 (2023)
54. M. Zhang, W. Sweeney, C. W. Hsu, L. Yang, A. D. Stone, and L. Jiang, Quantum noise theory of exceptional point amplifying sensors, *Phys. Rev. Lett.* 123(18), 180501 (2019)
55. F. Minganti, A. Miranowicz, R. W. Chhajlany, and F. Nori, Quantum exceptional points of Non-Hermitian Hamiltonians and Liouvillians: The effects of quantum jumps, *Phys. Rev. A* 100(6), 062131 (2019)
56. F. Minganti, A. Miranowicz, R. W. Chhajlany, I. I. Arkhipov, and F. Nori, Hybrid-Liouvillian formalism connecting exceptional points of non-Hermitian Hamiltonians and Liouvillians via postselection of quantum trajectories, *Phys. Rev. A* 101(6), 062112 (2020)
57. Y. X. Wang and A. A. Clerk, Non-Hermitian dynamics without dissipation in quantum systems, *Phys. Rev. A* 99(6), 063834 (2019)
58. Y. H. Kang, Y. Xiao, Y. Wang, Q. P. Su, and C. P. Yang, Dissipation-free approach for realizing non-Hermitian dynamics in a superconducting circuit, *Sci. China Phys. Mech. Astron.* 68(3), 230312 (2025)
59. V. V. Albert and L. Jiang, Symmetries and conserved quantities in Lindblad master equations, *Phys. Rev. A* 89(2), 022118 (2014)
60. F. Minganti, A. Biella, N. Bartolo, and C. Ciuti, Spectral theory of Liouvillians for dissipative phase transitions, *Phys. Rev. A* 98(4), 042118 (2018)
61. K. Macieszczak, M. Guta, I. Lesanovsky, and J. P. Garrahan, Towards a theory of metastability in open quantum dynamics, *Phys. Rev. Lett.* 116(24), 240404 (2016)
62. M. S. Sarandy and D. A. Lidar, Adiabatic approximation in open quantum systems, *Phys. Rev. A* 71(1), 012331 (2005)
63. N. Hatano, Exceptional points of the Lindblad operator of a two-level system, *Mol. Phys.* 117(15–16), 2121 (2019)
64. T. Prosen, Spectral theorem for the Lindblad equation for quadratic open fermionic systems, *J. Stat. Mech.: Theory Exp.* 07, P07020 (2010)
65. M. van Caspel, S. E. T. Arze, and I. P. Castillo, Dynamical signatures of topological order in the driven-dissipative Kitaev chain, *SciPost Phys.* 6, 026 (2019)
66. I. Frérot and T. Roscilde, Optimal entanglement witnesses: A scalable data-driven approach, *Phys. Rev. Lett.* 127(4), 040401 (2021)

67. S. Sayyad and F. K. Kunst, Realizing exceptional points of any order in the presence of symmetry, *Phys. Rev. Res.* 4(2), 023130 (2022)
68. D. Risté, M. Dukalski, C. A. Watson, G. de Lange, M. J. Tiggelman, Y. M. Blanter, K. W. Lehnert, R. N. Schouten, and L. DiCarlo, Deterministic entanglement of superconducting qubits by parity measurement and feedback, *Nature* 502(7471), 350 (2013)
69. S. Puri, A. Grimm, P. Campagne-Ibarcq, A. Eickbusch, K. Noh, G. Roberts, L. Jiang, M. Mirrahimi, M. H. Devoret, and S. M. Girvin, Stabilized cat in a driven nonlinear cavity: A fault-tolerant error syndrome detector, *Phys. Rev. X* 9(4), 041009 (2019)
70. W. Cai, Y. Ma, W. Wang, C. L. Zou, and L. Sun, Bosonic quantum error correction codes in superconducting quantum circuits, *Fundam. Res. (Beijing)* 1(1), 50 (2021)
71. X. Gu, A. F. Kockum, A. Miranowicz, Y. X. Liu, and F. Nori, Microwave photonics with superconducting quantum circuits, *Phys. Rep.* 718–719, 1 (2017)
72. A. F. Kockum and F. Nori, Quantum bits with Josephson junctions, in: Fundamentals and Frontiers of the Josephson Effect, Springer Series in Materials Science, Vol. 286, edited by F. Tafuri, Springer, 2019, Ch. 17, pp 703–741
73. J. Q. You and F. Nori, Atomic physics and quantum optics using superconducting circuits, *Nature* 474(7353), 589 (2011)
74. J. M. Martinis, S. Nam, J. Aumentado, and C. Urbina, Rabi oscillations in a large Josephson-junction qubit, *Phys. Rev. Lett.* 89(11), 117901 (2002)
75. R. Barends, J. Kelly, A. Megrant, A. Veitia, D. Sank, E. Jeffrey, T. C. White, J. Mutus, A. G. Fowler, B. Campbell, Y. Chen, Z. Chen, B. Chiaro, A. Dunsworth, C. Neill, P. O'Malley, P. Roushan, A. Vainsencher, J. Wenner, A. N. Korotkov, A. N. Cleland, and J. M. Martinis, Superconducting quantum circuits at the surface code threshold for fault tolerance, *Nature* 508(7497), 500 (2014)
76. H. Wang, M. Hofheinz, M. Ansmann, R. C. Bialczak, E. Lucero, M. Neeley, A. D. O'Connell, D. Sank, J. Wenner, A. N. Cleland, and J. M. Martinis, Measurement of the decay of Fock states in a superconducting quantum circuit, *Phys. Rev. Lett.* 101(24), 240401 (2008)
77. M. Hofheinz, H. Wang, M. Ansmann, R. C. Bialczak, E. Lucero, M. Neeley, A. D. O'Connell, D. Sank, J. Wenner, J. M. Martinis, and A. N. Cleland, Synthesizing arbitrary quantum states in a superconducting resonator, *Nature* 459(7246), 546 (2009)
78. T. Peronnin, D. Markovic, Q. Ficheux, and B. Huard, Sequential dispersive measurement of a superconducting qubit, *Phys. Rev. Lett.* 124(18), 180502 (2020)
79. M. A. Yurtalan, J. Shi, M. Kononenko, A. Lupascu, and S. Ashhab, Implementation of a Walsh–Hadamard gate in a superconducting qutrit, *Phys. Rev. Lett.* 125(18), 180504 (2020)
80. D. F. James and J. Jerke, Effective Hamiltonian theory and its applications in quantum information, *Can. J. Phys.* 85(6), 625 (2007)
81. C. M. Bender, M. V. Berry, and A. Mandilara, Generalized *PT* symmetry and real spectra, *J. Phys. Math. Gen.* 35(31), L467 (2002)
82. C. M. Bender, P. N. Meisinger, and Q. Wang, Finite-dimensional *PT*-symmetric Hamiltonians, *J. Phys. Math. Gen.* 36(24), 6791 (2003)
83. Q. H. Wang, 2×2 *PT*-symmetric matrices and their applications, *Philos. Trans. A Math. Phys. Eng. Sci.* 371(1989), 20120045 (2013)
84. B. Peng, Ş. K. Özdemir, F. Lei, F. Monifi, M. Gianfreda, G. L. Long, S. Fan, F. Nori, C. M. Bender, and L. Yang, Parity–time-symmetric whispering-gallery microcavities, *Nat. Phys.* 10(5), 394 (2014)
85. Y. L. Fang, J. L. Zhao, Y. Zhang, D. X. Chen, Q. C. Wu, Y. H. Zhou, C. P. Yang, and F. Nori, Experimental demonstration of coherence flow in *PT*- and anti-*PT* symmetric systems, *Commun. Phys.* 4(1), 223 (2021)
86. H. Xu, D. G. Lai, Y. B. Qian, B. P. Hou, A. Miranowicz, and F. Nori, Optomechanical dynamics in the *PT* and broken-*PT*-symmetric regimes, *Phys. Rev. A* 104(5), 053518 (2021)
87. Z. P. Liu, J. Zhang, K. Ozdemir, B. Peng, H. Jing, X. Y. Lu, C. W. Li, L. Yang, F. Nori, and Y. Liu, Metrology with *PT*-symmetric cavities: Enhanced sensitivity near the *PT*-phase transition, *Phys. Rev. Lett.* 117(11), 110802 (2016)
88. W. D. Heiss, The physics of exceptional points, *J. Phys. A Math. Theor.* 45(44), 444016 (2012)
89. G. Demange and E. M. Graefe, Signatures of three coalescing eigenfunctions, *J. Phys. A* 45(2), 025303 (2012)
90. C. M. Bender and S. Boettcher, Real spectra in non-Hermitian Hamiltonians having *PT* symmetry, *Phys. Rev. Lett.* 80(24), 5243 (1998)
91. C. M. Bender, Making sense of non-Hermitian Hamiltonians, *Rep. Prog. Phys.* 70(6), 947 (2007)
92. A. Guo, G. J. Salamo, D. Duchesne, R. Morandotti, M. Volatier-Ravat, V. Aimez, G. A. Siviloglou, and D. N. Christodoulides, Observation of *PT*-symmetry breaking in complex optical potentials, *Phys. Rev. Lett.* 103(9), 093902 (2009)
93. C. E. Rüter, K. G. Makris, R. El-Ganainy, D. N. Christodoulides, M. Segev, and D. Kip, Observation of parity–time symmetry in optics, *Nat. Phys.* 6(3), 192 (2010)
94. J. M. Torres, J. Z. Bernád, and G. Alber, Quantum teleportation and entanglement swapping of matter qubits with coherent multiphoton states, *Phys. Rev. A* 90(1), 012304 (2014)
95. K. Nemoto and W. J. Munro, Nearly deterministic linear optical controlled-not gate, *Phys. Rev. Lett.* 93(25), 250502 (2004)
96. S. D. Barrett, P. Kok, K. Nemoto, R. G. Beausoleil, W. J. Munro, and T. P. Spiller, Symmetry analyzer for nondestructive Bell-state detection using weak nonlinearities, *Phys. Rev. A* 71(6), 060302 (2005)
97. C. A. González-Gutiérrez and J. M. Torres, Atomic Bell measurement via two-photon interactions, *Phys. Rev. A* 99(2), 023854 (2019)
98. Z. Guo, J. Jiang, Y. Wang, J. Alvarez-Cuervo, A. T. Martin-Luengo, S. Hu, J. Jiang, P. A. Gonzalez, J. Duan, and H. Chen, Exceptional point empowered near-field routing of hyperbolic polaritons, *Sci. Bull.*

(Beijing) 69(22), 3491 (2024)

99. T. Brecht, Y. Chu, C. Axline, W. Pfaff, J. Z. Blumoff, K. Chou, L. Krayzman, L. Frunzio, and R. J. Schoelkopf, Micromachined integrated quantum circuit containing a superconducting qubit, *Phys. Rev. Appl.* 7(4), 044018 (2017)
100. S. Poletto, J. M. Gambetta, S. T. Merkel, J. A. Smolin, J. M. Chow, A. D. C'orcoles, G. A. Keefe, M. B. Rothwell, J. R. Rozen, D. W. Abraham, C. Rigetti, and M. Steffen, Entanglement of two superconducting qubits in a waveguide cavity via monochromatic two-photon excitation, *Phys. Rev. Lett.* 109(24), 240505 (2012)
101. D. I. Schuster, A. A. Houck, J. A. Schreier, A. Wallraff, J. M. Gambetta, A. Blais, L. Frunzio, J. Majer, B. Johnson, M. H. Devoret, S. M. Girvin, and R. J. Schoelkopf, Resolving photon number states in a superconducting circuit, *Nature* 445(7127), 515 (2007)
102. L. Sun, A. Petrenko, Z. Leghtas, B. Vlastakis, G. Kirchmair, K. M. Sliwa, A. Narla, M. Hatridge, S. Shankar, J. Blumoff, L. Frunzio, M. Mirrahimi, M. H. Devoret, and R. J. Schoelkopf, Tracking photon jumps with repeated quantum non-demolition parity measurements, *Nature* 511(7510), 444 (2014)
103. J. C. Curtis, C. T. Hann, S. S. Elder, C. S. Wang, L. Frunzio, L. Jiang, and R. J. Schoelkopf, Single-shot number-resolved detection of microwave photons with error mitigation, *Phys. Rev. A* 103(2), 023705 (2021)
104. Y. Jian, Y. Wang, Z. Guo, S. Hu, B. Wu, Y. Yang, and H. Chen, External excitation enabled chirality reversal of exceptional points in an effective anti-PT-symmetric non-Hermitian system, *Appl. Phys. Lett.* 123(14), 141702 (2023)
105. L. Hu, Y. Li, K. Zhu, H. Chen, and Z. Guo, Linewidth narrowing and enhanced sensing in non-Hermitian circuit systems via anti-PT symmetry, *Appl. Phys. Lett.* 126(9), 091702 (2025)
106. E. Jeffrey, D. Sank, J. Y. Mutus, T. C. White, J. Kelly, R. Barends, Y. Chen, Z. Chen, B. Chiaro, A. Dunsworth, A. Megrant, P. J. J. O'Malley, C. Neill, P. Roushan, A. Vainsencher, J. Wenner, A. N. Cleland, and J. M. Martinis, Fast accurate state measurement with superconducting qubits, *Phys. Rev. Lett.* 112(19), 190504 (2014)
107. J. Kelly, R. Barends, B. Campbell, Y. Chen, Z. Chen, B. Chiaro, A. Dunsworth, A. G. Fowler, I. C. Hoi, E. Jeffrey, A. Megrant, J. Mutus, C. Neill, P. J. J. O' Malley, C. Quintana, P. Roushan, D. Sank, A. Vainsencher, J. Wenner, T. C. White, A. N. Cleland, and J. M. Martinis, Optimal quantum control using randomized benchmarking, *Phys. Rev. Lett.* 112(24), 240504 (2014)
108. R. Barends, J. Kelly, A. Megrant, A. Veitia, D. Sank, E. Jeffrey, T. C. White, J. Mutus, A. G. Fowler, B. Campbell, Y. Chen, Z. Chen, B. Chiaro, A. Dunsworth, C. Neill, P. J. J. O'Malley, P. Roushan, A. Vainsencher, J. Wenner, A. N. Korotkov, A. N. Cleland, and J. M. Martinis, Superconducting quantum circuits at the surface code threshold for fault tolerance, *Nature* 508(7497), 500 (2014)
109. Y. H. Kang, Q. P. Su, Y. Wang, L. Shen, and C. P. Yang, Investigation of the topological quantum phase transition in a superconducting system via quantum walks, *Phys. Rev. A* 111(6), 062209 (2025)
110. M. A. Nielsen and I. L. Chuang, Quantum Computation and Quantum Information, Cambridge University Press, 2004
111. Y. Wang, Y. H. Kang, C. S. Hu, B. H. Huang, J. Song, and Y. Xia, Quantum control with Lyapunov function and bang-bang solution in the optomechanics system, *Front. Phys. (Beijing)* 17(3), 32501 (2022)
112. S. Liu, J. H. Shen, R. H. Zheng, Y. H. Kang, Z. C. Shi, J. Song, and Y. Xia, Optimized nonadiabatic holonomic quantum computation based on Forster resonance in Rydberg atoms, *Front. Phys. (Beijing)* 17(2), 21502 (2022)
113. Y. Xiao, Y. H. Kang, R. H. Zheng, J. Song, Y. H. Chen, and Y. Xia, Effective nonadiabatic holonomic swap gate with Rydberg atoms using invariant-based reverse engineering, *Phys. Rev. A* 109(6), 062610 (2024)
114. J. J. Burnett, A. Bengtsson, M. Scigliuzzo, D. Niepce, M. Kudra, P. Delsing, and J. Bylander, Decoherence benchmarking of superconducting qubits, *npj Quantum Inf.* 5, 54 (2019)
115. H. Paik, D. I. Schuster, L. S. Bishop, G. Kirchmair, G. Catelani, A. P. Sears, B. R. Johnson, M. J. Reagor, L. Frunzio, L. I. Glazman, S. M. Girvin, M. H. Devoret, and R. J. Schoelkopf, Observation of high coherence in Josephson junction qubits measured in a three-dimensional circuit QED architecture, *Phys. Rev. Lett.* 107(24), 240501 (2011)
116. A. Opremcak, C. H. Liu, C. Wilen, K. Okubo, B. G. Christensen, D. Sank, T. C. White, A. Vainsencher, M. Giustina, A. Megrant, B. Burkett, B. L. T. Plourde, and R. McDermott, High-fidelity measurement of a superconducting qubit using an on-chip microwave photon counter, *Phys. Rev. X* 11(1), 011027 (2021)
117. Y. Sung, L. Ding, J. Braumuller, A. Vepsalainen, B. Kannan, M. Kjaergaard, A. Greene, G. O. Samach, C. McNally, D. Kim, A. Melville, B. M. Niedzielski, M. E. Schwartz, J. L. Yoder, T. P. Orlando, S. Gustavsson, and W. D. Oliver, Realization of high-fidelity CZ and ZZ-free iSWAP Gates with a tunable coupler, *Phys. Rev. X* 11(2), 021058 (2021)
118. Y. H. Chen, W. Qin, X. Wang, A. Miranowicz, and F. Nori, Shortcuts to adiabaticity for the quantum Rabi model: Efficient generation of giant entangled cat states via parametric amplification, *Phys. Rev. Lett.* 126(2), 023602 (2021)